Appl. Phys. B 65, 375–391 (1997)

Applied Physics B Lasers and Optics

Visualisation of a supersonic free-jet expansion using laser-induced fluorescence spectroscopy: Application to the measurement of rate constants at ultralow temperatures

David J. Creasey[1], Dwayne E. Heard[1], Michael J. Pilling[1], Benjamin J. Whitaker[1], Martin Berzins[2], Roger Fairlie[2]

[1] School of Chemistry, University of Leeds, Leeds, LS2 9JT, UK
[2] Computational PDEs Unit, School of Computer Studies, University of Leeds, Leeds, LS2 9JT, UK

Received: 31 January 1997/Revised version: 24 March 1997

Abstract. Laser-induced fluorescence detection of the hydroxyl radical (OH) was used to measure the rotational temperature and the absolute gas density along the centreline of a continuous supersonic free-jet expansion. Measurement of the lifetime of the electronically excited state of OH with position in the expansion enabled the observed signal to be corrected for the effects of collisional quenching. Shock structures were observed with steep gradients in both temperature and density. The visualisation enabled fluorescence lifetimes taken inside the supersonic region to be used to obtain the rate constant for the quenching of $OH(A^2\Sigma^+, v' = 0)$ by air at 26 ± 4 K. A value of $2.56 \pm 0.40 \times 10^{-10}$ molecule^{-1}cm^{3}s^{-1} was obtained, a factor of more than four higher than at room temperature, and consistent with attractive forces dominating the quenching of $OH(A^2\Sigma^+)$. A detailed computational fluid dynamics (CFD) simulation of the supersonic free-jet expansion was performed, providing a two-dimensional visualisation of temperature and density variations throughout the expansion. The CFD calculations reproduced the salient features of the experimental temperature and density profiles along the centreline. Comparison between experiment and computation has allowed validation of CFD codes.

PACS: 32.50.+d; 82.20.Pm; 82.20.Wt

Free-jet expansions have been used by chemists, physicists, and engineers for many years in a variety of applications, including studies of photodissociation, elastic, inelastic, and reactive scattering in crossed molecular beams [1–3], the preparation of jet-cooled molecules for high-resolution spectroscopy [4, 5], the formation of van der Waals cluster molecules [6–8], the measurement of rate constants for ion-molecule quenching or charge transfer reactions at very low temperatures [9–11], and studies of aerodynamics [12].

In a relatively new application, we are employing a continuous supersonic jet expansion in order to detect ultra low concentrations of important trace radical species in the atmosphere [13]. In many molecular beam studies, a skimmer is placed in the supersonic region of the expansion in order to extract the centreline beam, with background pressures typically between 10^{-4} and 10^{-6} Torr. These experiments are not usually sensitive to the effect of shock structures, such as the Mach disc, involving rapid changes of temperature and density. However, this is not necessarily true of experiments in free jets, particularly with continuous sources with much higher background pressures, as employed in this work, and it is important to characterise the expansion. A feature of the Leeds experiment is the capability to probe the expansion from deep inside the supersonic region very close to the nozzle to well downstream of any shock structures [13]. Laser-induced fluorescence (LIF) detection of the hydroxyl radical (OH) is used as an *in situ* yet non-intrusive diagnostic of the expansion. Scanning the laser over several OH lines allows the rotational temperature to be measured at any point in the gas expansion, whereas the OH LIF signal and lifetime can be used to obtain the total gas density. The full visualisation of the free-jet expansion can be compared to the predictions of CFD models, allowing validation of the codes employed. LIF detection complements other diagnostic methods used for the visualisation of jet expansions, for example, pitot tube studies, Schlieren photography [14], and beam deflection optical tomography [15] for imaging of velocity and density gradients. *In situ* detection of chemical species throughout the evolution of a supersonic jet has been reported [2, 5, 9–11, 16] but is more widespread in the study of reactive flows, particularly flames [17–19], arc jets [20], and plasmas [21].

The free-jet offers potential for the study of collisional processes at ultra-low temperatures, but the density must be known to measure rate constants. Although it is relatively easy to measure the local translational temperature at any point in the expansion, the local number density and hence the collision rate varies with distance along the axis of the expansion. Smith and co-workers calculated gas temperatures and densities within a pulsed free-jet expansion[11] by solving the generalised Boltzmann equation, assuming an anisotropic Maxwellian distribution. Rate constants were determined for ion-molecule quenching and charge transfer reactions at the ultra-low temperatures ($T \geq 0.5$ K) calculated for the jet using the ion-monitor technique [9, 10]. The ions were generated at a point in the expansion where neutral-neutral collisions had effectively ceased. The calculations are complex and the densities not suitable for the study of neutral-neutral reactions.

Ion-molecule reactions have also been studied by the CRESU technique, developed by Rowe and co-workers at temperatures as low as 8 K [22]. The method relies on the formation of a uniform supersonic flow by means of an isentropic expansion of gas through a Laval nozzle. A collisional regime ensures that thermal equilibrium, and hence a meaningful temperature, is present within the expansion. More recently the technique has been extended to the study of neutral-neutral reactions [23], particularly for radical-radical reactions involving CN and CH, reaching temperatures as low as 13 K. There have been several theoretical predictions for the rates of radical-radical reactions at very low temperatures [24], and comparison with the CRESU results has proven fruitful. The CRESU technique, although successful, requires huge pumping capacities and the cost of the experiment is high. In addition only one temperature can be studied per Laval nozzle, which must be designed by calculation.

In this paper we show that by exploiting the relatively long fluorescence lifetime of the OH radical on the $A^2\Sigma^+$-$X^2\Pi_i$ transition, it is possible to determine the local density in a free-jet expansion where the quenching rates of OH are known. The magnitude of the LIF signal is then used to determine the density within the ultra-cold region of the expansion. Very good agreement between our experimental results and fluid-dynamics calculations indicate that it is possible to calculate reliably the properties of a free-jet expansion and hence obtain useful kinetic data at ultralow temperatures. This is illustrated by our determination of the rate constant for collisional quenching of electronically excited $OH(A^2\Sigma^+)$ at 25 K. The use of free-jets for such a measurement is only made possible by the visualisation of the variation of temperature and density in the expansion, both experimentally and by CFD modelling. Collisions of $OH(A^2\Sigma^+)$ with a number of species are known to occur on an attractive potential energy surface [25, 26] and thus the rate of quenching is expected to show an inverse dependence with temperature, as demonstrated by previous studies in cryogenically controlled cells [27], laser-heated cells [28], flames [29], and shock tubes [30]. No quenching measurements have been published at temperatures below 230 K, and the free-jet technique allows a straightforward means to study excited state dynamics at very low temperatures.

The paper is organised as follows. In Sect. 1 experimental details pertinent to the *in situ* probing of a molecular beam expansion are described. In Sect. 2 measurements of gas temperature and fluorescence lifetimes within different regions of the gas expansion from a variety of nozzle apertures are presented, together with the methodology for using these data to convert the observed LIF signal into a spatially resolved measurement of absolute density. In Sect. 3, the results of CFD calculations are presented, giving the two-dimensional variation of temperature, density and velocity, which are then compared with the experimental results. Finally, in Sect. 4, a methodology is described to obtain the rate constant for collisional quenching of the excited state of OH by air at the very low temperatures encountered in the jet expansion, using the density and lifetime data. Some discussion is given to the interpretation of the rate constant, which is an experimental quantity obtained directly from the data, given the anisotropic collisional environment that may be encountered within the jet expansion.

1 Experiment

An overview of the control structure of the experiment is given schematically in Fig. 1, being similar in design to that used by other groups measuring atmospheric OH [31–34]. Tuneable radiation at 308 nm is obtained using a copper vapour laser (CVL) (Oxford Lasers ACL-35) pumped dye laser (Lambda Physik LPD 3001). The CVL, configured with unstable resonator optics, is capable of operation at a pulse repetition rate up to 10 kHz and will deliver an output power in excess of 40 W at its optimal operating frequency of 7 kHz. For reasons of space the two lasers are configured one above the other on a double-decked table with the output beam from the CVL focused through a 1 mm spatial filter and collimated to a beam radius of about 8 mm as it is folded into the dye laser. The dye solution contains a mixture of Rhodamine 6G (0.15 gL^{-1}) and Rhodamine 640 (0.12 gL^{-1}) in ethanol, chosen to maximise output at 616 nm. This is frequency doubled using a KDP crystal, and the UV separated from the red fundamental by means of a standard assembly of four Pellin-Broca prisms. With an optimum input power into the dye laser of 20 W (sum of 511 nm and 578 nm lines), an output power of ~ 200 mw at 308 nm, or the equivalent of $\sim 30\,\mu J\ pulse^{-1}$ can be generated. The bandwidth of the laser at 308 nm, measured using the spectral profile of a single rotational line of OH at ~ 25 K, was found to be 0.25 cm^{-1} (the laser and gas beams are mutually orthogonal and hence Doppler broadening will be small, caused only by the radial component of the jet velocity) with a FWHM pulse length of 25 ns. The dye laser stepper motors for grating and doubling crystal are controlled via an IEEE GPIB interface from a PC. Cylindrical beam shaping and collimating optics generate a UV beam of ~ 3 mm diameter, whose pulse energy is controlled (without beam steering) by transmission through a Soleil-Babinet compensator and polarizer combination.

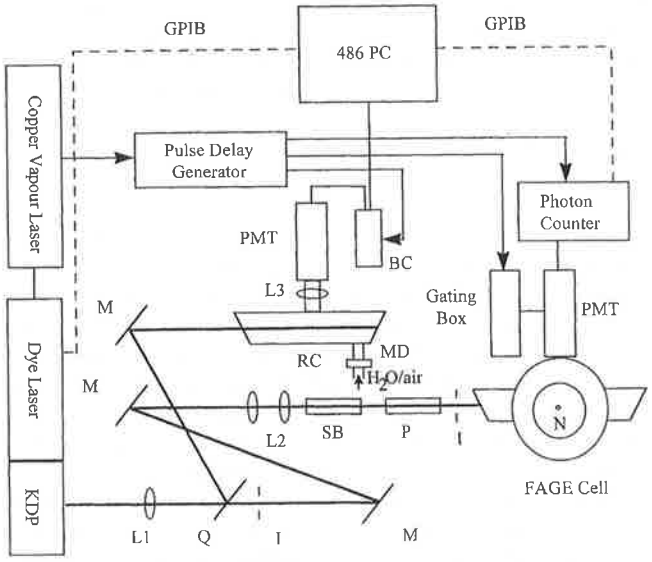

Fig. 1. Schematic diagram of the instrument for low-pressure LIF detection of OH. I, iris; N, nozzle; L1, cylindrical lens; L2, telescope; L3, condensing lens; SB, Soleil-Babinet compensator; P, polariser; M, mirror, Q, fused silica plate; PMT, photomultiplier; BC, boxcar integrator; RC, reference cell; MD, microwave discharge

A small fraction ($\sim 8\,\%$) of the UV beam prior to attenuation is directed into a reference cell using a fused silica beamsplitter. The reference cell consists of a small Pyrex discharge flowtube (internal diameter 22 mm), equipped with Brewster angle fused silica windows. A small flow of laboratory air is bubbled through deionised water and enters the flow-tube through a sidearm surrounded by a microwave discharge (EMS Microtron 200, 2450 MHz, 40 W). OH is generated in the discharge from the water vapour at a total pressure of ~ 9 Torr. The OH radical is excited in the $A^2\Sigma^+(v' = 0) \leftarrow X^2\Pi_i\ (v'' = 0)$ transition at ~ 308 nm, and fluorescence in the $(0,0)$ band is detected at right angles to the laser axis using a single collimating lens and a side-window PMT (RCA 1P28) masked by a UG11 filter. The PMT signal is sent directly to a gated integrator (Stanford Research Systems SR 250) whose output is digitised and stored on a PC. Analysis of LIF excitation spectra taken over the Q_1 branch shows the OH to be rotationally equilibrated at ambient temperature. The purpose of the reference cell is to maintain the laser wavelength at OH line centre whilst observing extremely low photon count rates in the main sampling cell. Small drifts in laser wavelength or pulse energy due to grating and doubling crystal instabilities (from temperature fluctuations) can be corrected using the reference signal.

Two cross-sectional views of the chamber are shown schematically in Fig. 2. It consists of a large, vertically orientated cylindrical chamber, with an internal diameter of 22 cm, mounted on a table separate from the optical bench. The laser beam with a typical pulse energy of $\sim 1\ \mu$J enters and exits the sampling chamber in the horizontal plane through two arms, each of length 35 cm containing a series of variously angled baffle rings with clear aperture of 7 mm, sealed with fused silica windows at Brewster's angle. The air sample containing OH enters the chamber through a nozzle vertically above the laser beam. The nozzle is mounted centrally within the flexible bellows of a stepper motor driven z-shift (Creative Vacuum Technology, DZSM/150/50, 40 mm range), which allows precise, reproducible control (± 0.001 in) of the laser-probed region along the vertical beam gas expansion. The nozzle position is computer controlled, and together with additional spacer flanges allows the vertical profile of the beam expansion to be interrogated from the nozzle to 232.5 mm downstream. A variety of flat plate nozzles have been used

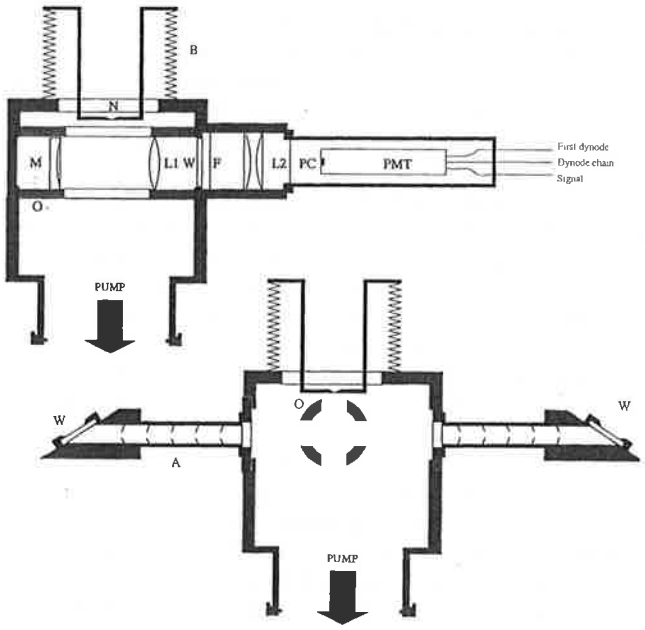

Fig. 2. Diagram showing two projections of fluorescence chamber. The excitation beam enters and exits the cell in the horizontal plane through the two long arms, each of 35 cm length and containing a series of variously angled baffle rings with clear aperture of 7 mm. The fluorescent light is collected at right angles to the excitation beam by means of a fl mirror/lens arrangement, which collimates the light through a narrow bandwidth interference filter. Condensing lenses are used to focus the light onto the photocathode of a fast photomultiplier tube. A, baffled arms; B, translatable bellows; F, 308 nm interference filter; L1, collimating lens; L2, condensing lenses; M, concave mirror; N, nozzle; O, optical rail; PC, 2.5 mm diameter photocathode; PMT, photomultiplier tube; W, fused silica window

with aperture diameters from 0.2 to 2 mm (Melles Griot, Ltd. and home-built from stainless steel plate) and a conical nozzle with 0.5 mm aperture (Molecular Beam Dynamics). The optimum cell pressure for OH detection in the atmosphere is ~ 1 Torr [31–34] and the high gas throughput to maintain this relatively low pressure in the detection chamber is provided by an Edwards E1200/E1M80 mechanical booster and rotary vacuum pump combination via an ISO 160 diameter bellows beneath the cell. The maximum pumping capacity is $\sim 225\ \mathrm{L\,s^{-1}}$, controlled by a VAT series 12 gate valve, and for a 1 mm nozzle maintains a cell background pressure of

Table 1. Experimental conditions for gas expansions using a variety of nozzles

Nozzle aperture d/mm	Background pressure p_b/Torr	Flow rate /sccm	Mach disc position Calculated[a]	x_m/mm Observed[b]	Mean free path[c] /mm	Asymptotic lifetime t/ns[d]
0.2	0.020	336	26.1	22–25[e]	2.5	690
0.5[f]	0.105	1573	28.5	f	0.46	620
0.6	0.176	2918	26.4	25	0.28	572
1.0	0.590	8521	24.1	24.5	0.08	393

[a] Calculated using (8).
[b] Using the observed rapid rise in temperature as an indication of the position of x_m.
[c] Calculated using the background pressure p_b and a temperature of 300 K.
[d] The lifetime is calculated using $\tau^{-1} = A_f + Q_f$ with $Q_f = \varrho_{in,b}\ k_{air}(300\ \mathrm{K})$, where $\varrho_{in,b}$ is the number density of the background air at pressure p_b, and $k_{air}(300\ \mathrm{K}) = 5.94 \times 10^{-11}$ molecule^{-1} cm^3 s^{-1}.
[e] There is no abrupt rise in temperature
[f] Skimmer of length 24 mm used as a conical nozzle, pointing away from the pump. It is experimentally impossible to probe the Mach disc region.

0.59 Torr (as measured with a 10 Torr capacitance manometer) with a linear gas velocity sufficient to ensure that the air sample at the probe region is replaced between laser shots (140 μs). The experimental conditions for a number of nozzle apertures are given in Table 1. In order to measure the total flow of air passing through a given nozzle aperture, a second vacuum cell with attached Pyrex flow-tube was placed over the nozzle. The flow of air, as measured by a variety of calibrated mass-flow controllers, was increased until the pressure in the second cell was equal to atmospheric pressure.

OH is artificially generated outside the sample cell. Laboratory air that is accelerated towards the nozzle is irradiated by a low-pressure mercury lamp (Oriel) with a fused silica envelope suspended ~ 2 cm above the nozzle. Radiation at 184.9 nm photolyses ambient water vapour generating OH with unit quantum yield. The concentration of water vapour is obtained from a humidity/temperature probe (Driesen and Kern). For some experiments synthetic air at atmospheric pressure with known (and variable) water vapour content flows down a fused silica flow tube, with the mercury lamp irradiating a known volume in the tube, prior to expansion at the nozzle. Chemical actinometry is employed to calibrate the OH concentration, with the mercury lamp masked by a 185 nm interference filter (Acton Research Corp.). Signals from OH concentrations as low as 6×10^6 molecule cm^{-3} outside the chamber have been calibrated, but for this work the OH concentration prior to the nozzle is ~ 10^{10}–10^{11} molecule cm^{-3}.

An end-window PMT tube with bialkali cathode (EMI 9893/100QB) situated perpendicular to the laser beam and the gas flow is used to detect the OH fluorescence. The PMT was specially selected for its low background count (< 20 cts s^{-1}) and small afterpulse signal, utilising a small effective photocathode diameter of 2.5 mm. A spherical mirror of 50 mm radius of curvature and 50 mm diameter is mounted on an optical rail inside the chamber along the optical axis of the PMT as a rear-reflector to double the solid angle of collected fluorescence (see Fig. 2). Along the same axis, also inside the cell, a 50 mm focal length f/1 fused silica condenser lens collimates the fluorescence, which then passes through a fused silica window and narrowband interference filter (Andover Corporation $\lambda_{max} = 310.9$ nm, FWHM bandwidth = 12 nm, 18 % transmission). The fluorescence is focused onto the 2.5 mm photocathode with two plano-convex lenses having a combined focal length of 37.5 mm, giving a magnification factor of 0.75 for the collection system. A region of 3–4 mm in diameter is thus imaged onto the PMT irrespective of the laser beam diameter, leading to good spatial resolution. The nozzle and its mount begin to block the solid angle subtended by the collection optics when the laser-to-nozzle distance is < 8 mm. Kinematic mounts and axial adjustments ensure that the optical components are optimally configured. Individual photon signals are counted directly using a two channel 200 MHz gated photon counter (SRS SR400). Alternatively, the entire temporal decay of the excited state can be captured using a multichannel scaler (SRS SR430), with a minimum temporal resolution of 5 ns. For a given channel of the photon counter two timing gates could be set: one was used to count the LIF photons and the other (at a long delay) to count scattered photons from the mercury lamp or ambient room light. In this manner background signals could be subtracted. The laser UV output is monitored with a photodiode and gated integrator assembly. The timing of the experiment is controlled by a digital delay/pulse generator (SRS DG535), with the firing of the copper laser acting as the master clock reference.

Fluorescence is collected at the same wavelength as the laser; hence great care must be taken to discriminate the weaker fluorescence signal from the more intense wall, Rayleigh, and Mie scattered light. In this work OH concentrations are sufficient that gated photon counting beginning ~ 40 ns after the laser pulse is able to eliminate scattered light effectively. For low concentrations of OH, afterpulse signals become noticeable. These are caused by photoelectrons from the intense laser scatter ionising residual gas (mainly H_2) in the PMT. The ions accelerated back onto the photocathode produce a secondary pulse which is amplified by the dynode chain in the PMT, falling within the OH fluorescence decay. These effects are minimised by gain switching of the PMT (using a home-built ~ 50 ns gating system [35]), which is turned off during the laser pulse.

2 Results

The signal excited from a quantum state i of ground state OH, given by S_i, in units of fluorescent photon counts s^{-1}, is proportional to the total OH number density $[OH]_o$ *outside the nozzle*. Assuming no heterogeneous losses in the nozzle itself, S_i is given by [32, 33]

$$S_i = [OH]_o C\, B_{fi} I \frac{1}{\sqrt{\Delta\upsilon_D^2 + \Delta\upsilon_L^2}} f_i \phi_f f_{gate} (\varrho_{in}/\varrho_{out}) , \qquad (1)$$

where:

- C is a constant that contains all terms associated with the fluorescence collection, namely, the overlap of the laser and gas beams, the solid angle over which fluorescence is collected, the transmission of lenses and filters, the quantum yield of the PMT, the discriminator setting of the photon counter, polarisation effects, and the laser probe volume. C does not change with position of the nozzle except when the nozzle begins physically to block the fluorescence collection volume ($x < 9$ mm).
- B_{fi} is the Einstein B coefficient for absorption from state i to state f.
- I is the laser power (all experiments are performed well away from optical saturation).
- $\Delta\upsilon_D$ and $\Delta\upsilon_L$ are the transverse Doppler width and the laser linewidth, respectively. The former, although weakly temperature dependent, is very small as the velocity component perpendicular to the jet flow axis is small (see Sect. 3 below).
- f_i is the fraction of the OH molecules that are in the rotational state i probed by the laser, which is given by

$$f_i = \frac{g_i \exp(-E_i/kT)}{Q(T)} , \qquad (2)$$

where g_i and E_i are the degeneracy and energy of state i, respectively, and $Q(T)$ is the partition function, summing over all spin-orbit and lambda-doublet levels. For either of the lambda-doublet levels of the lowest rotational level $N'' = 1$ of OH $^2\Pi_{3/2}$, $f_i \sim 4/Q(T)$, and thus is highly temperature dependent.

- ϕ_f is the fluorescence quantum yield of the excited state f, given by

$$\phi_f = \frac{A_f}{A_f + Q_f + P_f}, \tag{3}$$

where A_f, Q_f, and P_f are the state-specific radiative, quenching, and predissociation first-order rate constants, respectively. For $v'=0$, P_f is negligible except at extremely high rotational quantum numbers, and the values of A_f are known as a function of rotational state within the $A^2\Sigma^+$ $v'=0$ level [36–38]. The pseudo first-order quenching rate constant Q_f can be expressed as a sum:

$$Q_f = \sum_n [n] k_{f,n}(T), \tag{4}$$

where [n] is the number density of collider n that quenches OH in state f with a bimolecular rate constant $k_{f,n}(T)$. For the present experiments in air n = N_2, O_2, H_2O, and CO_2, with other constituents of air contributing negligibly to Q_f. The value of Q_f and hence ϕ_f is thus dependent upon the local density, temperature, and gas composition. The gas composition is assumed to be constant during the expansion and not affected by clustering or heterogeneous reactions. In the region probed by our experiments we see no evidence for the van der Waals OH–N_2 species. Clustering is further discussed in Sect. 2.2 below.

- f_{gate} is the fraction of the fluorescence signal that is collected by the gated photon counter and, using the notation of Holland et al. [33], is given by

$$f_{gate} = \exp\left(-\frac{\Delta T_c}{\tau}\right) - \exp\left(-\frac{\Delta T_c + T_c}{\tau}\right), \tag{5}$$

where ΔT_c is the delay of the start of the photon counter gate with respect to the laser pulse, T_c is the width of the photon counter gate, and τ is the fluorescence lifetime, given by

$$\tau = \frac{1}{A_f + Q_f}, \tag{6}$$

$$= \frac{\phi_f}{A_f}. \tag{7}$$

- Finally $\varrho_{in}/\varrho_{out}$ is the ratio of air density at a given point in the gas expansion to that outside the nozzle (the latter fixed by atmospheric conditions to be $\sim 2.5 \times 10^{19}$ molecule cm^{-3}). The value of ϱ_{in} will peak at the nozzle and generally decrease downstream, being dependent upon nozzle diameter and pumping speed, with discontinuities expected at shock fronts.

For constant laser power the first five terms on the RHS of (1) do not change with position within the expansion, whereas the remaining terms are strongly dependent upon the local temperature and density. An empirical approach was taken to determine the optimum signal level within the expansion by allowing the nozzle to be translated vertically with respect to the position of the detection axis. During these studies vertical profiles as a function of the distance from the nozzle to the detection axis were taken of (i) the rotational temperature, (ii) the fluorescence lifetime, and (iii) the OH signal, with a variety of detector temporal gates. From these measurements temperature and gas density profiles could be obtained along the central axis of the expansion with good spatial resolution, for comparison with the predictions of a CFD simulation.

2.1 *Gas temperature*

Accurate temperature determination is crucial for visualisation of the expansion and comparison with CFD calculations. A temperature profile is required to convert measured LIF intensities S_i to OH concentrations because of changes in the fraction f_i of the molecules in the absorbing level. Pointwise measurements of temperature were made both in the supersonic and subsonic regions of the expansion by scanning the dye laser to excite fluorescence from several rotational levels of OH $^2\Pi_{3/2}$ using the $Q_1(1)$ to $Q_1(4)$ lines, their satellites, and the $P_1(1)$ line of the (0, 0) band between 615.675 and 616.690 nm. The distribution of the ground state rotational populations is used to determine the rotational temperature.

If temperatures are to be measured using LIF, care must be taken to ensure that rotational level dependent processes, for example, quenching rate constants, do not cause the parameters that determine the LIF signal via (1) to change with the rotational level probed [39]. Changes in these parameters with rotational level would lead to erroneous relative ground state populations and hence temperature. The exception is the absorption coefficient, which changes with rotational level, but which is accurately known for each rotational transition. A judicial choice of experimental conditions was chosen so that the measured temperature reflected the distribution amongst rotational levels only. The absence of optical saturation for all lines was checked in two ways; first by variation of the laser power and observation of a linear response of the LIF signal, and second by comparison of the intensity ratio of the Q_1 lines to their satellite Q_{21} lines (which probe the same upper $\Pi(A')$ lambda doublet level in $N''=1$); in all cases this was equal to the ratio of Einstein absorption coefficients [40, 41].

The rate constant for quenching decreases with the rotational quantum number that is excited within OH $A^2\Sigma^+$, $v'=0$ [42], and for N_2 at 300 K the change is 25 % in going from $N'=1$ to 4 [42]. For the values of $\Delta T_c = 50$ ns and $T_c = 1000$ ns used in the temperature measurement, and assuming a typical beam density of 3×10^{16} molecule cm^{-3} (typical for the 1 mm nozzle, see Sect. 2.2 below) this leads to a change of the product of the quenching terms $\phi_f \times f_{gate}$ of ~ 10 % between exciting $Q_1(1)$ and $Q_1(4)$. In reality the change will be less than this, due to equilibration within $A^2\Sigma^+$ $v'=0$ by rotational energy transfer (RET) prior to quenching. The rate of RET out of a single rotational level to other levels within $A^2\Sigma^+$, $v'=0$ is much faster than the rate of quenching from that level (following excitation of $N'=4$ the ratio is ~ 10 for air [43, 44].) The $v'=0$ level is thus largely thermalised prior to quenching, and changes in quenching rate are only a very small source of error for the temperature measurement. It is also important to avoid spectral biasing that may result from a change in the fluorescence spectrum of OH with excited rotational level. The interference filter used in this work ensures a sufficiently wide spectral bandpass of 12 nm. Self-absorption of the OH fluorescence can be ignored at the concentrations and path lengths used in this work.

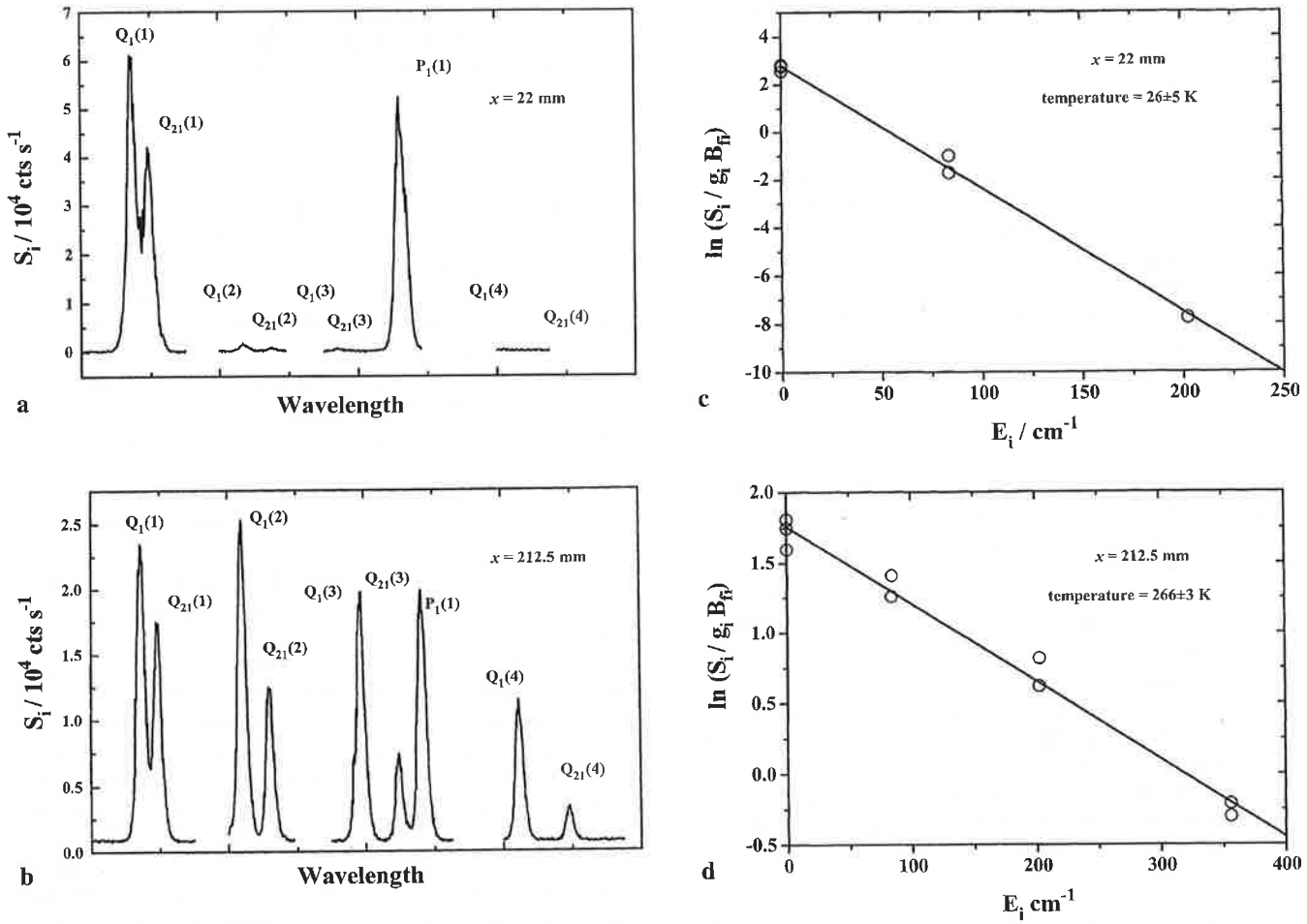

Fig. 3a–c. Laser excitation spectrum in the Q_1 branch region of the OH $A^2\Sigma^+(v'=0)$–$X^2\Pi_i$ $(v''=0)$ transition near 308 nm, taken at **a** $x = 22$ mm and **b** $x = 212.5$ mm downstream of a flat nozzle with 1 mm diameter aperture, with a background pressure of 0.59 Torr and backing pressure of 760 Torr. The concentration of OH in the chamber is $\sim 1 \times 10^8$ molecule cm^{-3}, generated by a Hg lamp outside the chamber. The UV laser energy used was 900 nJ per pulse, with the ratio of main-branch to satellite line intensities confirming the absence of optical saturation. The spectrum, taken with a grating step resolution of 0.006 nm, with 1 s (7000 shots) averaging, is not normalised for changes in laser power, but with the continuous wave contribution due to scatter from the photolysis lamp subtracted. The discontinuities arise because the laser wavelength is rapidly slewed between rotational lines. The values of the gating parameters ΔT_c and T_c used were 55 and 1000 ns, respectively. Boltzmann plots of $\ln\{S_i/(B_{fi}g_i)\}$ vs. rotational energy E_i for the spectra in (**a**) and (**b**) are shown in **c** and **d**, respectively. The gradients yield rotational temperatures of 26 ± 5 K and 266 ± 3 K at $x = 22$ and 212.5 mm respectively, with the errors representing 2σ from the linear least squares fit to the data

Figure 3a, b shows laser excitation spectra taken at two positions within a gas expansion from a 1 mm aperture in a flat plate (referred to as the 1 mm nozzle). The spectra were analysed in two ways. First, integrated line intensities were divided by the appropriate value of B_{fi}, which is calculated from rotational line strengths and transition probabilities, the latter including the variation of transition dipole moment with internuclear distance [45], and the level degeneracy, g_i, which is given by $2N'' + 2$ for the $^2\Pi_{3/2}$ manifold. The result is plotted in logarithmic form vs. rotational energy (data taken from [46]) in Fig. 3c, d. The gradients of the so-called Boltzmann plots yield the rotational temperatures. Second, the software package LIFBASE [41], developed at SRI International, was used to generate simulated spectra at different user-defined temperatures until the best fit with experiment was obtained. Good agreement was obtained between the methods. It should be noted that the population for $N'' = 1$ derived from the intensity of either the of $P_1(1)$ or $Q_1(1)$ lines was the same, ruling out any significant non-equilibrium lambda-doublet populations. Collisional alignment of molecular rotation has been observed in seeded expansions of CO_2 [47], O_2 [48], and I_2 [49] but preferential alignment of the molecular axis of OH parallel to the flow of the jet should not introduce a significant error in the measured temperature. Experiments are in progress to probe this alignment. All spectra analysed yielded linear Boltzmann plots, indicating that the rotational populations would appear to be described reasonably by a thermal distribution.

Figure 3a–d immediately demonstrates that a wide range of rotational temperatures are encountered in the beam. Figure 4a-d shows the rotational temperature, obtained from Boltzmann analyses, vs. the nozzle-to-laser distance x, for 0.2, 0.6, and 1.0 mm (flat) and 0.5 mm (conical) nozzles, respectively. The background cell pressure and gas flow rates through the nozzle in each case are given in Table 1. The vertical spatial resolution for each measurement, defined by the imaging optics and photocathode diameter, is ~ 3 mm (the laser-beam diameter was also kept at ~ 3 mm). Increased

scattered light and physical blocking of the fluorescence collection volume by the nozzle mount prevent accurate measurements closer than ~ 9 mm from the nozzle. In the case of the 0.5 mm conical skimmer, measurements were not possible less than 33 mm from the aperture because of the impossibility of probing inside the upward pointing nozzle. Scans were taken along the centreline expansion axis of the LIF signal with the laser wavelength fixed on both the $Q_1(1)$ and $Q_1(2)$ lines. The ratio of signals for a given value of x enabled a continuous measure of the temperature to be found using known Einstein B coefficients and assuming similar quenching for each excited state, confirming the sharp rises in temperature shown in Fig. 4a–d.

For all of the nozzles studied, the ratio $\varrho_{out}/\varrho_{in}$ exceeds the critical value for the gas flow speed to reach the local speed of sound at the nozzle [50]. The gas will cool during the expansion and in the supersonic region does not sense the downstream boundary conditions. If the background pressure in the chamber were very low, the jet would evolve to molecular flow conditions and no shock structure would be observable in the chamber. Such conditions are common for most spectroscopic and dynamical studies using jet expansions. However, for the background pressures used in this work, the jet must adjust to the continuum flow at the boundaries and a series of shock fronts is encountered, which are thin regions of gas with steep gradients in density, temperature, and velocity. The shock wave at the side of the jet parallel to the centre line is called the barrel shock, whereas the shock normal to the centreline is called the Mach disc, at which point the flow becomes subsonic. Further discussion of these features is given in Sect. 3 below. The position of the Mach disc, x_m measured in nozzle diameters d, is given approximately by [50]

$$\frac{x_m}{d} = 0.67\sqrt{\frac{p_o}{p_b}}, \tag{8}$$

where p_o is the pressure outside the nozzle, p_b is the background pressure in the chamber, and d the nozzle diameter. The local jet pressure is close to the background pressure at

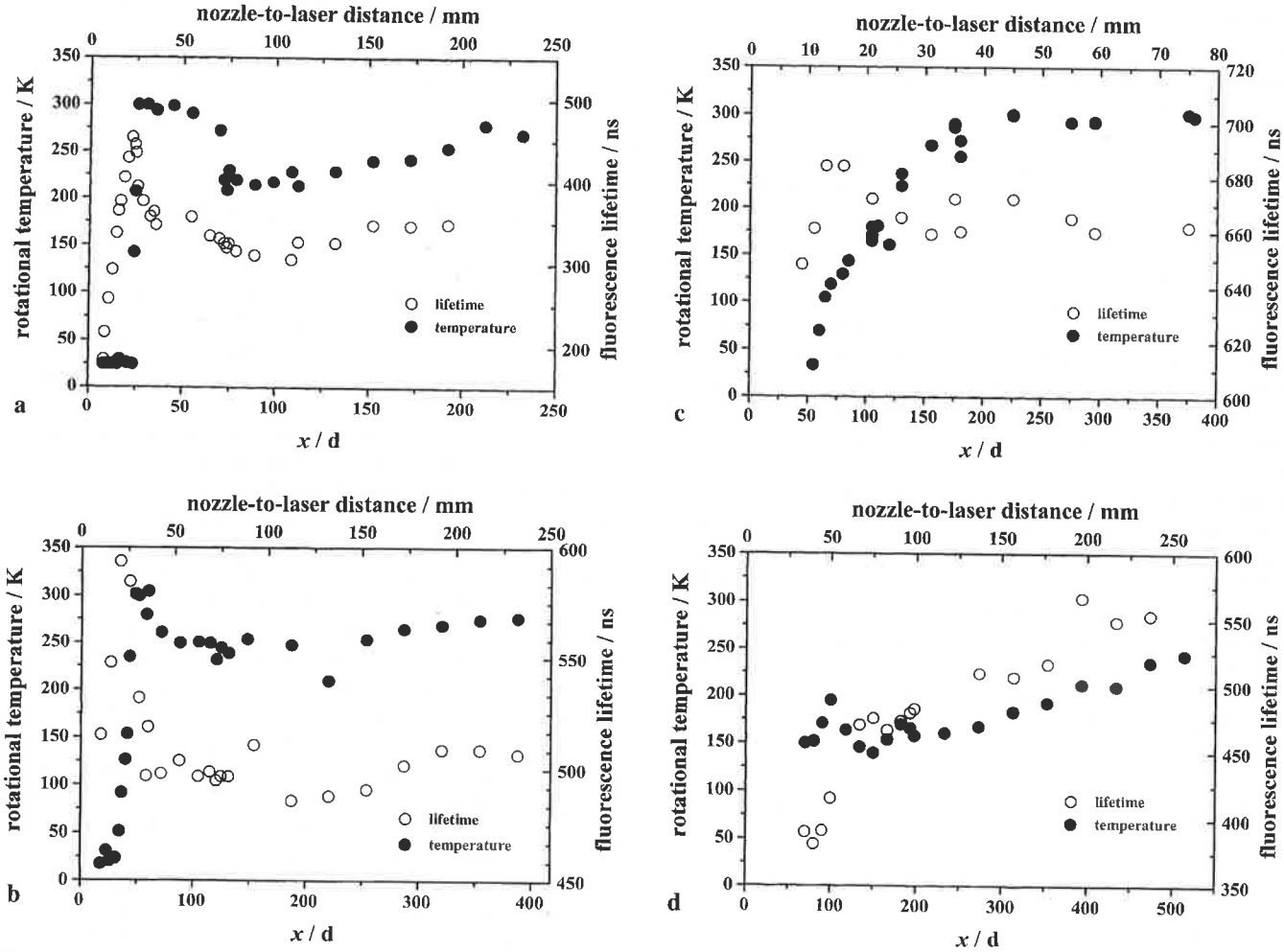

Fig. 4. Rotational temperatures (filled circles, left hand axis) obtained from Boltzmann analyses of LIF excitation spectra, and fluorescence lifetimes (open circles, right hand axis) as a function of x, the distance downstream from a variety of nozzles with apertures d. **a** flat nozzle (machined stainless steel disc, thickness 0.33 mm) with drilled aperture of diameter 1 mm; **b** flat nozzle (Melles Griot, thickness 0.013 mm) with 0.6 mm aperture, mounted on stainless steel disc; **c** flat nozzle (Melles Griot, thickness 0.013 mm) with 0.2 mm aperture, mounted on stainless steel disc; **d** conical skimmer (Molecular Beam Dynamics), length 24 mm, aperture 0.5 mm, pointing into the flow. $x = 0$ corresponds to the nozzle itself, and the spatial resolution of the measurements is about 3 mm. Increased scattered light prevents measurements very close to the nozzles. Error bars are omitted for clarity, being close in size to the symbols. For temperature measurements typical 2σ errors are between 2 and 8 K, whereas for the lifetimes, typical 2σ error bars are between 1 and 8 ns

the Mach disc position. Calculated values of x_m are tabulated in Table 1. The diameter of the Mach disc normal to the centre line is given approximately by 0.5 x_m [50], which for all nozzles used in this work corresponds to a volume considerably larger than that imaged onto the PMT.

For the 1 mm nozzle, Fig. 4a indicates a rise in temperature from 25–281 K occurring between $x = 24$ and 25 mm. This agrees well with the calculated position of the Mach disc of 24.1 mm using (8), and to the position calculated by CFD (see Sect. 3 below). The thickness of the Mach disc is likely to be about one mean free path, which is given in Table 1 for the *background* conditions of each expansion. In 0.59 Torr of air at 300 K (the background gas conditions for the 1 mm nozzle expansion) the value is ~ 0.1 mm, but because of spatial averaging inherent in the experiment the observed temperature rise occurs over a mm or so. Inspection of Fig. 4b shows the jump in temperature to be less abrupt for the 0.6 mm nozzle, but again the observed and calculated Mach disc position are still in good agreement. The 0.2 mm nozzle (Fig. 4c) shows a rise in temperature from 25–300 K between 12 mm (the closest distance studied for this nozzle) and ~ 40 mm. Equation (8) predicts the Mach disc at 26.1 mm, and the mean free path for the background conditions is ~ 2.5 mm, but clearly the temperature rise occurs over a much wider range of x/d, indicating that little or no shock structure is present. For the 0.5 mm aperture conical skimmer (Fig. 4d), it is not possible to probe the supersonic region and observe any Mach disc shock structure because the nozzle blocks the beam. Following what is expected to be substantial cooling (together with shock structure), a relatively slow return to ambient temperatures is observed.

Comparison can be made with other groups who employ continuous jet expansions to measure atmospheric OH. Holland *et al.* [33] measured a rotational temperature of 207 K 70 mm from a 0.75 mm aperture conical nozzle, whereas Stevens et al. [32] calculated the translational temperatures (based on pitot tube studies of the flow velocity) of 245 and 298 K at 114 and 214 mm, respectively, from a 0.93 mm aperture flat nozzle. Although the gas flows, cell pressures, and pumping speeds were different to those used in this work, the results indicate that substantial cooling is to be expected during monitoring of atmospheric OH. It is possible that the flow downstream of the Mach disc may re-expand, and the velocity once again becomes supersonic. Indeed, from Pitot tube studies Stevens et al. [32] report a supersonic flow 114 mm downstream of the nozzle. For both the 1 mm and 0.6 mm flat nozzles it is clear from Fig. 4a–b that temperatures well below ambient are observed downstream of the Mach disc, and this point is further discussed in Sect. 3 below.

2.2 *Gas density*

Rearrangement of (1) gives the density of air within the expansion:

$$\varrho_{in} = \frac{D\, S_i}{f_i \phi_f f_{gate}}, \tag{9}$$

where

$$D^{-1} = [OH]_o C B_{fi} I \frac{1}{\sqrt{\Delta v_D^2 + \Delta v_L^2}} \frac{1}{\varrho_{out}}, \tag{9a}$$

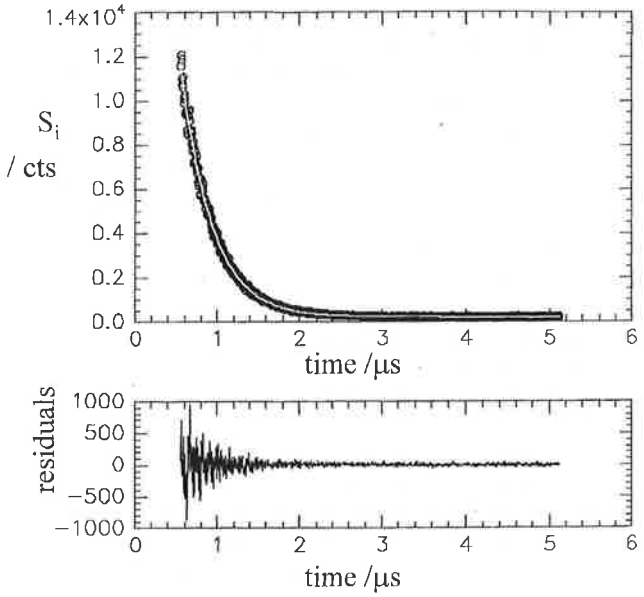

Fig. 5. Upper panel: Fluorescence decay from OH $A^2\Sigma^+$, $v' = 0$ following $Q_1(1)$ excitation recorded at 5 ns resolution with a multichannel scaler, averaging over 2.5×10^5 laser shots. The data were taken with the laser at 36 mm from a 1 mm aperture flat nozzle. The laser (FWHM 25 ns) was fired at $t = 410$ ns, and the large peak due to laser scatter has been removed. The solid white line shows an exponential fit to the data, yielding $\tau = 362 \pm 4$ ns (2σ error). Lower panel: residuals to the nonlinear least squares fit

is a collection of the terms from (1) that, for a given laser power, are constant with distance from the nozzle. Knowledge of the temperature profile allows f_i to be calculated as a function of x, but in order to calculate ϕ_f and f_{gate} from (3) and (5), respectively, the fluorescence lifetime is required. In addition, to obtain an absolute profile of density, ϱ_{in}, from a profile of signal, S_i, it is also necessary to know the value of D.

Figure 5 shows the fluorescence decay following $Q_1(1)$ excitation at 36 mm from the 1.0 mm flat nozzle, taken at 5 ns resolution. The early part of the decay, which also contains the scattered light peak, has been removed. The residuals following a nonlinear least squares fit of an exponential function to the data are shown in the lower panel, with the fit yielding a lifetime of $\tau = 362 \pm 4$ ns, the error representing 2σ. Excitation via $Q_1(1)$ initially populates the $N' = 1$ state, and using the total RET rate constant for energy transfer measured for the constituents of air [43], together with a beam density of $\sim 3 \times 10^{16}$ molecule cm^{-3}, it is estimated that the rotational levels within $v' = 0$ will thermalise to the local translational temperature during the early part of the observed fluorescence lifetime. Potential distortion of the early part of the decay due to saturation of the PMT or by RET were ruled out by fitting different portions of the decay and obtaining the same lifetime. As well as temperature profiles, Fig. 4a–d also shows the fluorescence lifetimes following $Q_1(1)$ excitation as a function of the centreline laser-to-nozzle distance x for each nozzle studied.

There have been several experimental [36–38] and theoretical [51–53] determinations of the radiative lifetime, τ_{rad}, of the $A^2\Sigma^+ v' = 0$ excited state of OH. The radiative lifetime is a function of the rotational level, but as fluorescence is observed from several rotational levels following RET, an

average value of $\tau_{rad} = 709$ ns ($A_f = 1.41 \times 10^6\ s^{-1}$) is used in this work. From Fig. 4 it is seen that the fluorescence lifetime varies with position within the expansion for all nozzles studied. This is because of changes in the quenching rate with position, which at large values of x/d tends to an asymptote reflecting the quenching by air at the background chamber pressure. The lifetime, τ, is given by

$$\tau = \frac{1}{A_f + Q_f} = \frac{1}{A_f + \sum_n [n] k_{f,n}(T)} = \frac{1}{A_f + \varrho_{in} k_{air}(T)}, \quad (10)$$

where $k_{air}(T) = \sum_n x_n k_{f,n}(T)$ is an effective bimolecular rate constant for quenching by air, with x_n the mole fraction of atmospheric species n, and $\sum_n [n] = \varrho_{in}$ the density at a given position in the expansion.

For the 1 mm nozzle the fluorescence lifetime is 184 ± 8 ns at $x = 8.5$ mm and steadily increases to 453 ± 4 ns at $x = 24$ mm, just before the Mach disc. The temperature and hence $k_{air}(T)$ is constant over this region and the increase in lifetime thus reflects the decrease in density. Interestingly, at no point does the lifetime approach the natural lifetime, implying there are sufficient collisions to cause significant quenching of the excited state. The rate constant for the rotational relaxation of low-lying levels of OH $X^2\Pi_i$ $v'' = 0$ is $\sim 10^{-10}$ molecule cm^{-3} [54], somewhat higher than the value for quenching of the excited state [27, 55]. The fact that the lifetime continues to increase with x is evidence that the system is in thermodynamic equilibrium, even though the temperature has reached a constant value, and is consistent with the linear nature of the Boltzmann plots. At the Mach disc the lifetime is seen to decrease rapidly, to 356 ns at 33 mm, reflecting an increase in Q_f, but the contribution to Q_f due to a rise in density at the shock front is offset somewhat by the expected decrease in the value of $k_{air}(T)$ between 25 and 300 K. After the Mach shock the lifetime then decreases again, most probably because of the increase in k_{air} as the temperature falls to around 210 K, rather than a further increase in the density. The CFD calculations (see Sect. 3 below) give a jet flow velocity of ~ 65 m s^{-1} downstream of the Mach disc (which converts to 0.065 mm vertical movement in 1 μs), and hence "fly-out" of the fluorescence collection volume does not contribute to the observed fluorescence decay. Inside the Mach disc the CFD calculations predict that the axial jet velocity rises to ~ 750 m s^{-1} (0.75 mm in 1 μs) at $x = 10$ mm, remaining fairly constant until the Mach disc. Again, fly-out will not contribute significantly to the lifetimes observed.

Similar behaviour is observed for the 0.6 mm nozzle, where a 100 ns reduction in τ is observed at the Mach disc, the larger values of τ compared to the 1 mm nozzle reflecting the lower density of the bath. For the 0.2 mm nozzle τ is close to τ_{rad} at all distances, even close to the nozzle where the jet velocity is high, providing further experimental evidence that fly-out is not contributing significantly to any of the observed fluorescence decays. Using the background pressure measured with the capacitance manometer, and the room temperature value of $k_{air} = 5.94 \times 10^{-11}$ molecule^{-1} $cm^3 s^{-1}$, calculated using known quenching rate constants for N_2, O_2, CO_2 and H_2O [27, 55], the asymptotic values of Q_f and hence τ can be calculated for each nozzle. These values are given in Table 1, and agree well with the experimental values (Fig. 4a–d) obtained at large values of x/d.

Figure 6a–c shows the variation of the signal S_i with distance from the nozzle for the 1, 0.6, and 0.2 mm flat nozzles, respectively. The nozzle was stepped 0.2 mm between points, and S_i represents the counts due to LIF signal alone, with the contribution from laser and mercury lamp scatter removed.

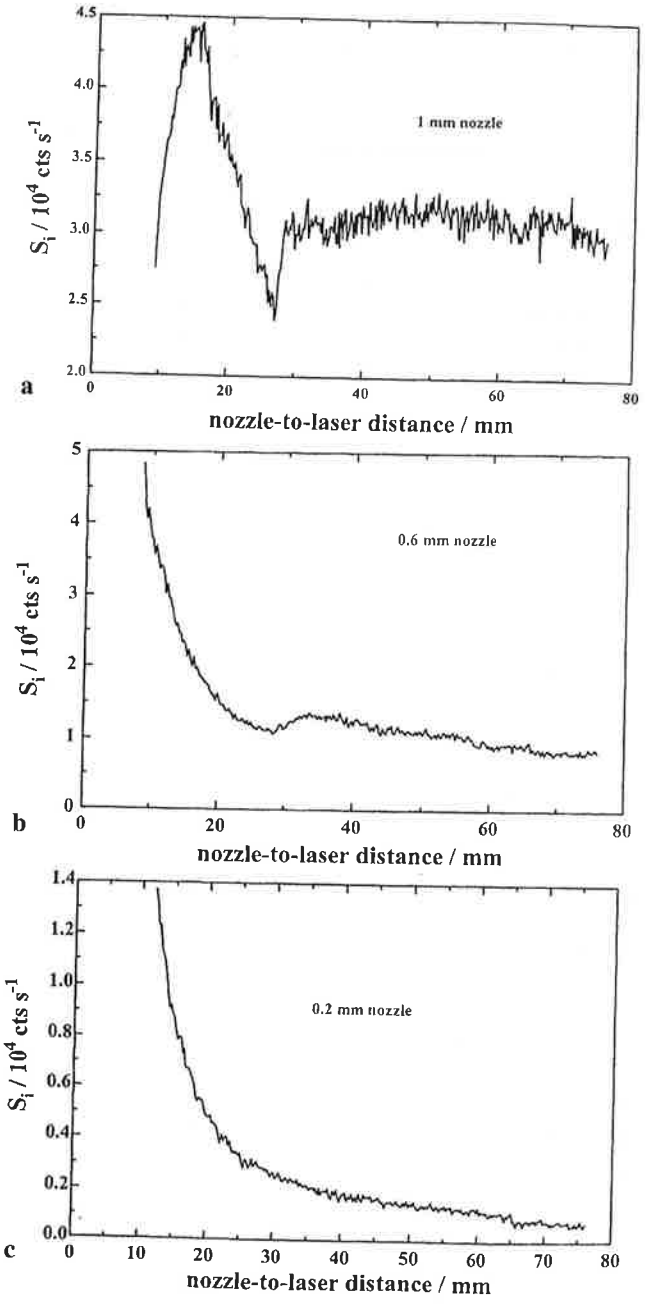

Fig. 6. Variation in the OH fluorescence photon count rate (S_i) as a function of the distance from the nozzle to the laser axis, for **(a)** 1 mm, **b** 0.6 mm, and **(c)** 0.2 mm aperture nozzles mounted on flat plates. The nozzle was stepped 0.2 mm between points, averaging for 7000 laser shots per point. S_i represents the counts due to LIF signal alone, with the contribution from laser and mercury lamp scatter removed. The count rates for each nozzle should not be compared as no attempt was made to keep the laser power constant between scans. In each case the photon counter gating parameters employed were $\Delta T_c = 55$ ns and $T_c = 1000$ ns, which enables capture of most of the fluorescence lifetime

The count rates for each nozzle should not be compared as no attempt was made to keep the laser power constant between scans. In each case the photon counter gating parameters employed were $\Delta T_c = 55$ ns and $T_c = 1000$ ns , which capture most of the fluorescence lifetime except just after the laser pulse. At large values of x (>150 mm) the signal begins to drops off, presumably due to chemical loss or dilution by mixing with background gas containing little or no OH. Further discussion is limited to data taken at laser to nozzle distances less than 75 mm. In the general case the signal appears to decrease initially with distance from the nozzle before reaching a fairly constant value. Structure due to the Mach disc shock at $x \sim 25$ mm is clearly visible for the 1 mm nozzle data, is less so for the 0.6 mm nozzle data, but is absent for the 0.2 mm nozzle. The behaviour for the 1 mm nozzle signal at distances close to the nozzle deserves further attention. Figure 7a,b show for this nozzle the variation in the signal count rate S_i between 8 and 36 mm taken with the photon counter gate parameters of (**a**) $\Delta T_c = 55$ ns, $T_c = 1000$ ns (referred to as "long") and (**b**) $\Delta T_c = 45$ ns, $T_c = 50$ ns (referred to as "short"), respectively, with the laser power similar for each scan. Also shown on each graph is the product $\phi_f \times f_{gate}$, calculated from (3) and (5) for each detection gate, representing the total effect upon S_i from quenching of the excited state. It can be seen that for the "short" gate (Fig. 7b), the product is fairly constant (within 20 %), reflecting that changes in quenching conditions have little effect on the signal. The value of S_i is lower in Fig. 7b than in Fig. 7a since f_{gate} is small for the short gate. Except very close to the nozzle, $\Delta T_c/\tau$ and $(\Delta T_c + T_c)/\tau$ are small for (**b**), and hence (5) can be reduced to $f_{gate} \sim T_c/\tau = T_c(A_f/\phi_f)$, making $\phi_f \times f_{gate}$ independent of the collisional environment, as reflected by Fig. 7b. Differences in the choice of gating parameters are most evident very close to the nozzle. Indeed for the "long" gate conditions (Fig. 7a), the signal initially rises with increasing distance from the nozzle, even though the OH number density is decreasing as the gas expands. Clearly in this region the dependence of the signal S_i on local quenching conditions is stronger than the dependence upon OH number density. There are no partition function effects as the temperature is constant for this range of x. At $x \sim 16$ mm the variation of S_i with x is slight, a reflection that the dependence on OH number density and quenching cancel one another, but above $x = 16$ mm the signal is controlled more by OH number density. Such effects are not observed for the 0.6 mm or 0.2 mm nozzle data in the probed region $x > 8$ mm as the overall quenching rate is much smaller.

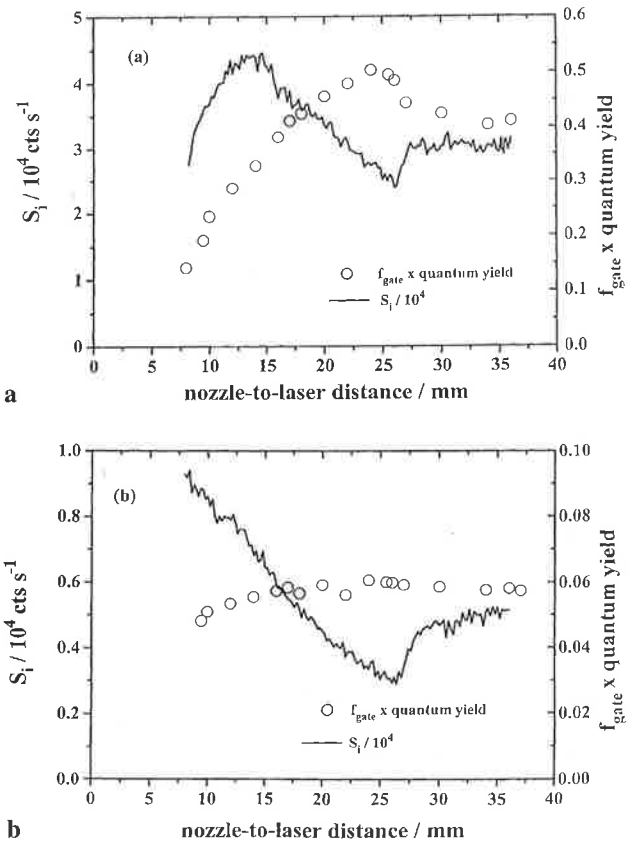

Fig. 7. Variation of the photon count rate S_i as a function of distance between the nozzle and the laser for the flat 1 mm nozzle for photon counter gate settings of (**a**) $\Delta T_c = 55$ ns, $T_c = 1000$ ns (referred to as "long") and (**b**) $\Delta T_c = 45$ ns, $T_c = 50$ ns (referred to as "short"). The laser power was approximately the same for each scan and each point represents the average of 7000 shots. Shown also on each graph (right hand axis) is the product $\phi_f \times f_{gate}$ representing the effect of quenching on the signal (see text for details)

In principle, measurement of the lifetime at any point and hence the quenching rate, Q_f, can yield the absolute density, ϱ_{in}, directly from (10), if the rate constant for quenching is known. The rate constant for quenching of $v' = 0$ following $Q_1(1)$ excitation has been measured in this laboratory for the atmospheric colliders N_2, O_2, and CO_2 between 236 and 298 K in a discharge-flow system [56]. The results agree well with previously published data [27], and together with the rate constant for quenching by water vapour (for which data are available only at room temperature [55]) and its measured mixing fraction, allows an effective bimolecular rate constant for quenching by air, $k_{air}(T)$, to be calculated. The contribution to Q_f from CO_2 quenching is negligible, whereas for H_2O is ~ 10 % for a volume mixing fraction of 1 %. The error in using the 300 K value for $k_q(H_2O)$ rather than the true (but unknown) value at lower temperatures is therefore small (< 2 %). The mole fraction of water was obtained from the measured humidity and temperature of the gas entering the nozzle. Thus, at any point within the expansion where $T \geq 236$ K, the value of ϱ_{in} can be found *directly* from the lifetime τ via (10) once $k_{air}(T)$ has been calculated. In this calculation it is assumed that the collisions with air are those of an isotropic gas sample, enabling a thermal rate constant, $k_{air}(T)$ to be used.

For the 1 mm nozzle, the density was obtained via this procedure for 19 points within the expansion for $25 < x < 192.5$ mm. Unfortunately, it is not possible to obtain the density directly from τ in the supersonic region as the value of $k_{air}(T)$ at the ultralow temperatures observed is not known. However, it should be possible to obtain ϱ_{in} at *any* position in the expansion from (9) using a scan of signal S_i vs. nozzle-to-laser distance if the constant D is known, since the values of f_i, ϕ_f, and f_{gate} can be calculated from the temperature and lifetime data using (2), (3), and (5) respectively. Because ϱ_{in} is already known for isolated positions within the expansion from the lifetimes, D can be calculated from the signal S_i at these points. Figure 8 shows the value of the constant D (for "long" gating) as a function of x for the 1 mm nozzle, the data

exhibit a standard deviation of ~ 6 % between 25 and 70 mm. The constant value of D implies that any thermal anisotropy that may lead to an error in the determination of the absolute density from the lifetime is not changing with distance down the jet. By using the mean value of D, it is now possible to determine the variation in density directly from (9) in both the supersonic and sonic regions of the expansion from a scan of the signal S_i recorded as a function of laser-to-nozzle distance x. Figure 9 shows the absolute density ϱ_{in} (in units of molecule cm^{-3}) between 8.5 and 72 mm, calculated from (9), using the value of D obtained as explained above. The "long" detector gate parameters were used, but a very similar density profile was obtained using the signal obtained from the "short" gate.

A rapid increase in density at the shock front is expected, marking the transition between the supersonic region and the background conditions within the chamber. At the Mach disc, the temperature suddenly rises (Fig. 4a), and as the laser is probing the lowest rotational level ($^2\Pi_{3/2}$ $N'' = 1$), the fraction of molecules in the probed state suddenly falls as population is transferred to higher levels. The observed signal, however, does not change appreciably as the density has risen sharply. The fraction, f_i, appears in the denominator of (9) describing the total density ϱ_{in}, and as the other terms do not change appreciably at the Mach disc (including the observed signal), is entirely consistent with the rise in density. After the Mach disc none of the parameters on the RHS of (9) change appreciably, as ϱ_{in} is fairly constant. The concentration of OH outside the nozzle is known from calibration experiments, and hence the OH density (summed over all quantum states) at any point in the expansion can also be found, being related to ϱ_{in} by $[OH]_{in}=[OH]_o(\varrho_{in}/\varrho_{out})$. This is shown on the right hand axis in Fig. 9 for $[OH]_o = 1 \times 10^{11}$ molecule cm^{-3}. Clearly for field measurements it is not desirable to excite OH fluorescence close to the Mach disc, as any optical alignment instabilities or changes in ambient pressure may lead to significant fluctuations in the observed signal. Over the range of x studied it should be noted that the total OH density peaks after the Mach disc, even though the observed LIF signal (probing $N'' = 1$ of $^2\Pi_{3/2}$), and hence the sensitivity of the instrument for OH detection, peaks inside the supersonic expansion (see Figs. 6a and 7a), where f_i is at its maximum.

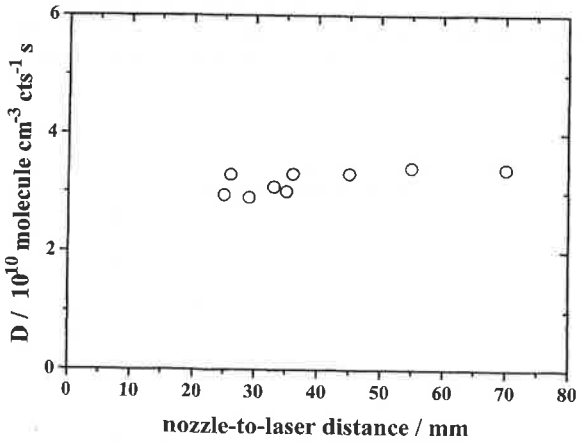

Fig. 8. Variation of the experimental constant D [defined by (9a)] as a function of position within the expansion from a flat 1 mm nozzle. The value of D was calculated from (9), utilising the measured value of S_i obtained with "long" gating parameters of $\Delta T_c = 55$ ns and $T_c = 1000$ ns, and the values of ϱ_{in}, f_i, ϕ_f, and f_{gate} calculated from measured temperature/lifetime data and known rate constants for quenching

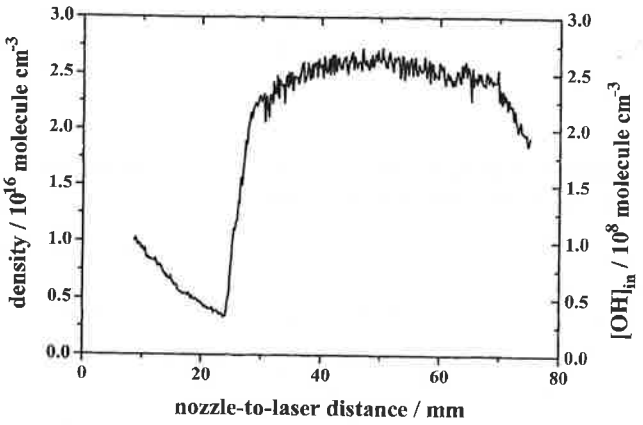

Fig. 9. Variation of the absolute density ϱ_{in} (in units of molecule cm^{-3}) between 8.5 and 72 mm from the 1 mm flat nozzle, calculated from (9) as explained in the text. The left hand axis gives the total density in the beam, in, and the right hand axis gives the absolute OH number density, $[OH]_{in}$, calculated using the known, calibrated mixing fraction of OH entering the nozzle

A similar analysis was applied to the data shown in Fig. 6b,c for the 0.6 and 0.2 mm nozzle expansions respectively to obtain the absolute total and OH number density profiles. For the 0.2 mm nozzle, little or no shock structure was observed, with the density monotonically decreasing with distance. For the 0.6 mm nozzle the density profile was similar to that of the 1 mm nozzle but with a less pronounced increase at the Mach disc. The asymptotic densities were close to the values calculated from the observed background temperature and pressure.

The LIF signal from a given ambient OH concentration will be reduced if clusters are formed between OH and atmospheric colliders. The OH-N_2 van der Waals cluster has been observed and characterised spectroscopically by Giancarlo *et al.* [57] using LIF in a supersonic jet expansion of photolysed HNO_3, Ar, and N_2 mixtures. The conditions employed were vastly different to those in this work, a stagnation pressure of ~ 4 bar with considerably lower background pressure was used. The OH was generated *in situ* inside the vacuum chamber, with the complex observed by exciting in the (1 , 0) region of OH near 282 nm, but no corresponding features were observed in the 0,0 region. The binding energy of the OH ($X^2\Pi_i$)-N_2 complex was not measured directly but was estimated at ~ 400 cm^{-1} [57]. Two unassigned features were observed by Giancarlo et al. [57] 400 cm^{-1} above the OH $P_1(1)$ line in the 0-0 band, but a search at this wavelength in the supersonic region of the 1 mm nozzle expansion in this laboratory revealed no signal attributable to OH clusters. Such a result is not surprising; the rotational temperature in this work is higher than that reported by Giancarlo et al. [57], and the OH number density is probably considerably lower, making observation of clusters difficult. Binary or higher clusters with water are more likely to form [58] but these have not been detected spectroscopically and hence the loss of OH via complexation with water cannot be assessed. Recently Hofzumahaus et al. [34] reported that the sensitivity of the Julich instrument designed for atmospheric OH meas-

urements was found to be a function of $[H_2O]$ incident at the nozzle, perhaps caused by H_2O condensation in the gas expansion.

3 CFD Calculations and comparison with experimental temperature and density profiles

The experimental temperature and density profiles recorded for a variety of nozzle diameters (with known boundary conditions) provide a unique opportunity to test stringently the predictions of a CFD calculation for a supersonic free-jet expansion. The aim of performing CFD calculations on the expansion of ambient air as it passes through the nozzle into the gas beam is to describe fully the spatial variation in temperature, density, and velocity along the beam. The cylindrical symmetry inherent in the problem reduces the three-dimensional problem to one involving the axial (x) and radial (r) distances from the nozzle.

The physical situation to be considered is that of a region of high pressure gas (p_o) which is separated from a region of low pressure gas (p_b). If a nozzle connects the two regions then gas from the high pressure region will escape into the low pressure region and if the pressure ratio $P_r = p_o/p_b$ between the two regions is large enough then the velocity at the nozzle exit becomes locally sonic. The pressure at the nozzle exit at this time remains greater than the background chamber pressure and the gas must continue expanding into the ambient region, and is said to be an underexpanded jet [50].

Figure 10 illustrates the complicated pattern of shocks which form as expansion waves reflect from the jet boundary, calculated for $P_r = 7.52$, much lower than the values studied experimentally. A characteristic Mach disc that is normal to the jet axis separates the supersonic jet core from the downstream subsonic jet core. The intersection of the Mach disc with the interior jet boundary shock produces a triple point

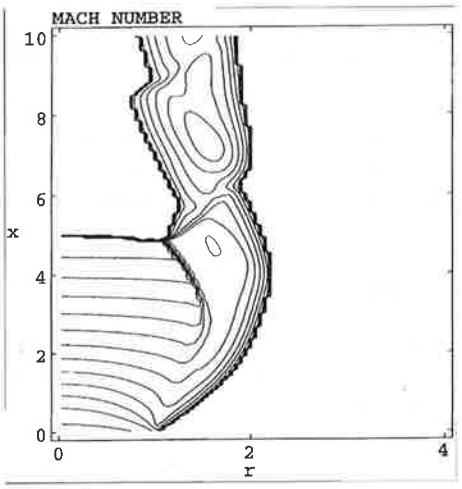

Fig. 10. A plot of contour lines representing Mach numbers for a typical jet, with a ratio of pressures between the nozzle exit and the background of 7.52. As the jet is cylindrically symmetric about $r = 0$ only half the jet is illustrated. The diagram does not represent conditions used at Leeds and is used to illustrate the major features of a supersonic jet expansion. The contours are linearly spaced from Mach 1 to Mach 4.34, and the values of the axial (x) and radial (r) distances are arbitrary. The Mach disc and barrel shocks are clearly evident, at which point the contours are very closely spaced

and further reflections downstream. In certain instances these are strong enough to produce a sonic throat forcing the interior of the jet to become supersonic again. This can then produce repeating Mach disc structures downstream.

The mathematical model of this situation consists of the two-dimensional Euler inviscid equations in axisymmetric geometry [59]:

$$\frac{\partial \boldsymbol{U}}{\partial t} + \frac{1}{r}\left(\frac{\partial (r\boldsymbol{F})}{\partial r}\right) + \frac{\partial (r\boldsymbol{G})}{\partial x} = \boldsymbol{T}\,, \tag{11}$$

where $\boldsymbol{U}$ is a vector of conserved quantities, and $\boldsymbol{F}$ and $\boldsymbol{G}$ the corresponding fluxes. These equations represent conservation of mass, energy, and momentum in the radial and axial directions. The vectors for an inviscid gas are

$$\boldsymbol{U} = (\varrho, \varrho v_r, \varrho v_x, e)\,, \tag{12}$$

$$\boldsymbol{F} = \left[\varrho v_r,\ p + \varrho v_r^2,\ \varrho v_r v_x,\ v_r(e+p)\right]\,, \tag{13}$$

$$\boldsymbol{G} = [\varrho v_x,\ \varrho v_r v_x,\ p + \varrho v_x^2,\ v_x(e+p)]\,, \tag{14}$$

where p is the pressure, ϱ is the density, v_r and v_x are the flow velocity in the radial and axial directions, respectively, and e is the total energy per unit volume, defined by

$$e = \frac{p}{\gamma - 1} + \frac{1}{2}\varrho(v_r^2 + v_x^2)\,, \tag{15}$$

where γ is the ratio of specific heat capacities for air ($\gamma = 1.4034$). $\boldsymbol{T}$ is a vector of source terms given by

$$\boldsymbol{T} = \left(0, \frac{p}{r}, 0, 0\right)\,. \tag{16}$$

In the cases of interest here we are looking for steady-state solutions of the (11), that is, for which $\delta \boldsymbol{U}/\delta t = 0$.

The computational domain is shown in Fig. 11. The size of this domain is dependent upon the particular case being studied, particularly with regard to the pressure ratio, P_r. The larger this pressure ratio, the larger the domain needs to be to accommodate the position of the Mach disc and the width of the jet, both of which increase with increasing pressure ratio. The boundaries of the domain need to be treated with care. While the inner radial boundary and the $x = 0$ axial boundary are simple to model, the other two boundaries (downstream

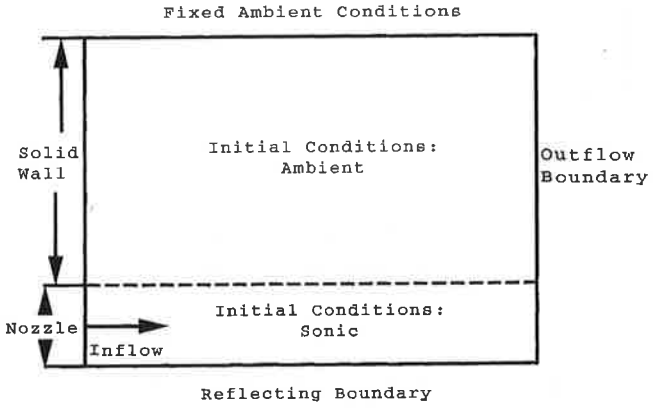

Fig. 11. The computational domain used in the CFD calculations

and outer radial) are more tricky. The axial boundary can simply be set to be a reflective boundary while the $x = 0$ boundary is set to be solid apart from the jet inflow position, which contains fixed information about the jet. The outer radial boundary is very important since it is from this boundary that the jet "learns" about the ambient conditions. This boundary is set to be have the experimental pressure and density. The gas at this boundary is also set to be at rest, and its position must be chosen carefully. If it is too close to the axis then the shock structure may intersect it, which may cause the code to break down; if it is too far from the axis, then the computational time taken for the ambient conditions to affect the jet may be excessive. Finally the downstream boundary condition must be considered. This boundary condition must be able to adapt to whether the flow is subsonic or supersonic. Should the local flow be supersonic at the downstream boundary, then the information criterion means that the flow at the boundary cannot be influenced by the downstream conditions. However, if the outflow is subsonic, then the flow is influenced by the downstream conditions. To solve this, an imposed pressure is substituted as the resolved pressure in the numerical boundary conditions as described below.

The initial conditions are chosen to minimise the amount of computational time required to obtain a steady solution. A band, the same width of the jet and set to be the same as the jet inflow conditions, stretches across the domain. The conditions that the jet inflow must be set to, in particular the pressure, are not easy to calculate. While the pressure outside the nozzle is known, the pressure at the nozzle exit is unknown. Estimates in the literature suggest a drop of 50 % in pressure through the nozzle [50]; however, these estimates fail to take into account the shape of the nozzle. This is important as the position that sonic flow is achieved will vary according to the nozzle shape. The thickness of the 1 mm flat nozzle is 0.33 mm. For the purposes of this simulation, at each pressure ratio a separate model of the nozzle was run to obtain a steady flow through the nozzle. Pressure drops in the region of 40 % were found.

The numerical solution of (11) is calculated using a time marching finite volume scheme from standard computational fluid dynamics techniques [60]. The computational domain is divided into cells of fixed size Δr and Δx (radial and axial directions, respectively) whose size and number depend upon the precise problem being solved. These values are given in Table 2. The particular spatial discretisation method used is that of a cell-centred finite volume scheme [61], in which the cell centroid is assigned the mean value of the conserved values in that cell. The scheme is second order in smooth regions and first order at discontinuities. The integral form of the conservation equation is discretised in a standard finite volume approach, resulting in the need to evaluate the flux functions on the mid-point of the cell edges. The code here is a variant [62] on the well-known Godunov scheme [63, 64], which uses the solution of a Riemann problem to determine physically correct flux values on the edges, given two different sets of solution values from the cells on either side of the edge. In regions where the solution is rapidly changing an exact first-order Riemann solver is employed [65] in other regions, it is sufficient to make use of a linear approximation to the solution [66]. The integration from time t to $t + \delta t$ is then achieved using the forward Euler method with the time step limited by the Courant–Friedichs–Lewy (CFL) condition [64].

In the case of the imposed pressure boundary the Riemann solver is given the values of the interior cell as well as the imposed pressure. This imposed pressure is taken as the resolved solution in the Riemann problem, which enables the resolved velocity and density values to be calculated. The values at the interface are then calculated from the resolved solution in the normal manner.

Steady solutions were obtained for jets with pressure ratios $P_r = 200$, 452 and 1288, the third case corresponding to the conditions for the 1 mm flat nozzle ($p_b = 0.59$ Torr), for which profiles of temperature and density were obtained experimentally. CFD calculations for smaller nozzle diameters, and hence higher values of P_r, were not attempted, as the times for convergence were expected to be prohibitively long. The solution for temperature within the 1 mm nozzle jet expansion is shown in Fig. 12. The plots of density, pressure, and Mach number are similar for this nozzle. The region of very low temperature is clearly evident (point A in

Table 2. Gridding parameters used in CFD calculations[a]

Nozzle diameter	P_r	r_{size}/mm	x_{size}/mm	Δr/mm	Δv/mm	No. of cells
2 mm	200.52	5	150	0.25	0.25	12000
1.5 mm	452.38	7	200	0.2	0.2	35000
1 mm	1288.14	13	150	0.25	0.25	31200

[a] P_r is the pressure ratio, defined by p_o/p_b, where p_o and p_b are the pressure outside the nozzle and the background pressure in the chamber, respectively. r_{size} and x_{size} are the total domain size in the radial and axial directions, respectively, and Δr and Δx are the cell sizes in these two orthogonal directions.

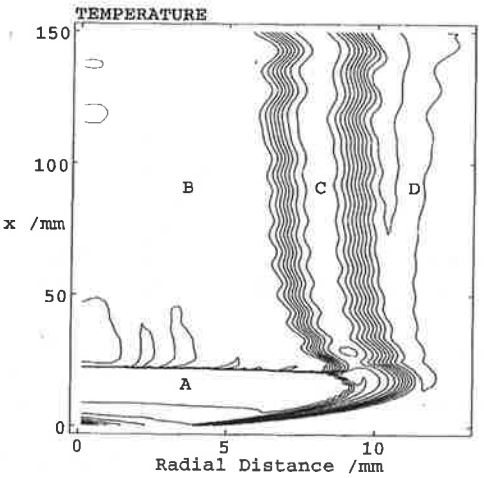

Fig. 12. CFD calculation of the temperature field for an expansion with a pressure ratio $p_o/p_b = 1288$, corresponding to the experimental conditions for the flat 1 mm nozzle. Once again, as the expansion is symmetric about $r = 0$, only $r > 0$ is shown. The vertical axis is the axial distance downstream of the nozzle, with the nozzle at $x = 0$. The nozzle is situated on the horizontal axis between the radial distances of $r = -0.5$ and 0.5 mm. There are 17 linearly spaced contours between 10 K and 348 K. The temperature at four points within the expansion is given: A, 10 K; B, 300 K; C, 119 K; and D, 321 K. The Mach disc shock at $x \sim 25$ mm, just downstream of point A, and the barrel shock at around $r = 8$–10 mm, are clearly evident. It should be noted at for $x > 25$ mm, if a slice is taken across the jet (for example from B to D), the temperature drops from ambient to ~ 120 K before returning to ambient values at the edge of the jet

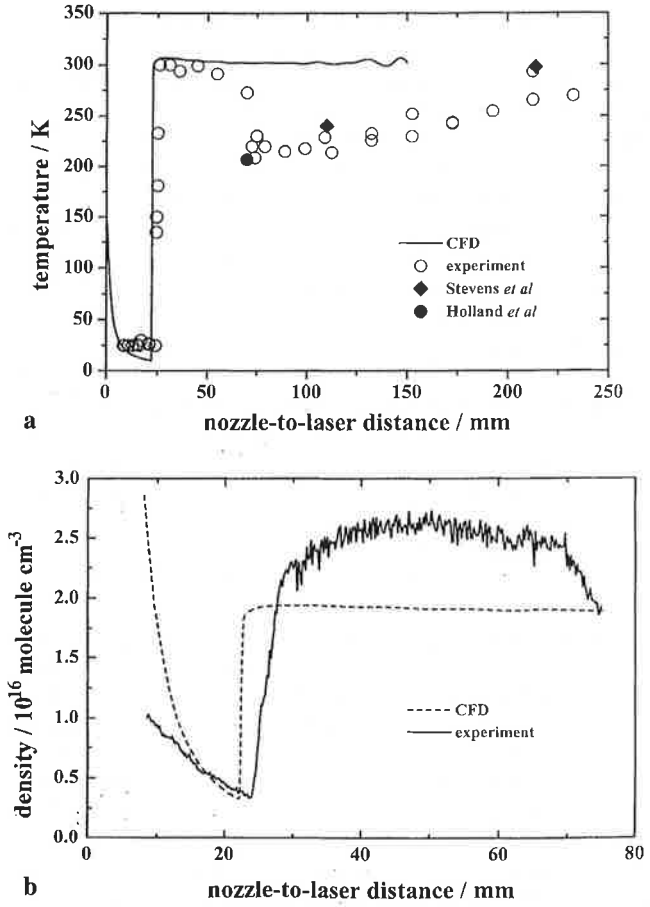

Fig. 13. Comparison of the (**a**) temperature, and (**b**) density profiles as a function of axial distance from a 1 mm nozzle, as predicted by the CFD calculations and measured experimentally. For the CFD, sufficient cells have been averaged in order to reflect the experimental spatial resolution. Two isolated temperature measurements by Stevens et al. [32] and Holland et al. [33] are also shown in (**a**). The CFD calculations were only performed out to $x = 150$ mm

Fig. 12), and the width of the barrel shock (8–10 mm) is large enough to ensure that in the radial direction the probed region of gas ($\sim$ 1–2 mm either side of the centre line $r = 0$) does not contain large temperature or density gradients. The CFD code also outputs the axial and radial velocity of the gas for each cell. For the 1 mm nozzle the axial velocity increases from 300 m s^{-1} at the nozzle exit to 750 m s^{-1} before the Mach disc, dropping to an approximately constant value of $\sim$ 65 m s^{-1} afterwards. At no point beyond the Mach disc do the CFD calculations predict that the jet becomes supersonic again.

In order to provide a validation of the two-dimensional visualisation of the expansion given by CFD the experimental data of centreline rotational temperature and density of air within the jet are utilised, as given in Figs. 4a and 9. The raw data are laser excitation spectra, fluorescence lifetimes, and signal magnitude as a function of nozzle-to-laser beam distance, all taken with a spatial resolution of $\sim$ 3 mm, corresponding to $r = \pm 1.5$ mm. Figure 13a,b shows the CFD temperature and density profiles respectively along the centreline, averaged between $r = 0$ and 1.5 mm in order to reflect the experimental spatial resolution. Superimposed on Fig. 13 is the experimental data for the 1 mm nozzle. CFD predicts the Mach disc to be at $\sim$ 23 mm from the nozzle, close to the experimentally observed value of $x_m = 24$–25 mm. Although not experimentally measured in this work, the radii of the barrel shock and the Mach disc have been measured for free-jet expansions using light scattering techniques and are of the order ($\pm$25 %) of 0.375 x_m ($\sim$ 9 mm) and 0.25 x_m ($\sim$ 6 mm), respectively [50], consistent with the CFD predictions shown in Fig. 12. Along the centreline, the CFD calculation does not predict the drop in temperature that is observed experimentally at $x \approx 75$–80 mm (Fig. 4a), followed by a slow rise to 300 K. It is not clear why this cooling is observed experimentally. One explanation is that cooler air present between the barrel shock and the jet boundary (point C in Fig. 12) is being mixed into the air at the centreline. Profiles of temperature across the jet indicate steep temperature gradients at the barrel shock, but since the CFD code does not describe a viscous, turbulent model, mixing processes are not included. The asymptotic density is set by the boundary conditions of the chamber, but the general shape of the density profile predicted by CFD (Fig. 13b) is similar to that observed experimentally. Further discussion of the density is given in Sect. 4 below. Refinements of the model to incorporate viscosity and turbulence (and hence mixing) would improve the accuracy of the predictions. CFD calculations that employ adaptive gridding, but which are still in progress, indicate that some cooling may occur beyond the Mach disc shock.

The CFD calculations assume an expansion of a perfect gas with a ratio of specific heat capacities $\gamma = 1.4034$ (the value for air [67], which is close to the classical value for a linear molecule with active rotations only). The CFD calculations do not include internal degrees of freedom and output the translational temperature, ignoring rotational to translational energy transfer that will occur during the expansion. If there are sufficient collisions throughout the expansion to maintain thermal equilibrium, then if the calculations are accurate, the CFD temperature and the OH rotational temperature should approach one another. For the 1 mm nozzle, the experimental radiative lifetime is always much less than the natural lifetime, indicating a collisional environment. For $x <$ 24 mm, there is a region where the temperature is extremely low ($\sim$ 25 K) and relatively constant, whereas CFD predicts a monotonic decrease in temperature, reaching a minimum of 10 K immediately prior to the Mach disc. The agreement is reasonable considering the hard-sphere approximation of the calculations.

4 Determination of the quenching rate constant for quenching of OH($A^2\Sigma^+$, $v' = 0$) by air at ultralow temperatures

Upstream of the mach disc ($x < 24$ mm) the observed value of the density, ϱ_{in}, and the OH lifetime, τ, can be utilised to obtain the rate constant for quenching by air at the local temperature of $\sim$ 25 K. Such a measurement would be extremely difficult using a cell that is cryogenically cooled, and studies within a gas expansion offer potential for measurement of kinetic parameters at ultralow temperatures [9–11]. It is important, however, to assess the effect of any disequilibrium between the rotational and translational degrees of freedom or any anisotropy in the distribution of collision velocities [11], as discussed above. Rearranging (10), a Stern–Volmer plot

of the inverse lifetime, τ^{-1}, vs. density, ϱ_{in}, for the region where the temperature is constant yields a slope of $k_{air}(T)$ and an intercept of A_f. Figure 14 shows such a plot for data taken using the 1 mm nozzle. Increasing air density on the plot corresponds to moving closer to the nozzle inside the Mach disc shock. The plot is linear up to a beam density of $\sim 9 \times 10^{15}$ molecule cm^{-3} ($\sim$ 11 mm from the nozzle), and a linear-least squares fit to the data in this region yields $k_{air} = (2.56 \pm 0.40)\ 10^{-10}$ molecule^{-1} cm^3 s^{-1} (2σ errors) at an average rotational temperature of 26 K. The intercept of $(1.20 \pm 0.30)\ \times 10^6$ s^{-1} is consistent with the literature value of A_f, which is in the range $1.3\text{–}1.6 \times 10^6$ s^{-1} [36–38, 51–53]. The quoted error represents 2σ taking only statistical errors into account. The errors in the lifetimes are small (1–2 %), and the errors in the derived value of the absolute gas density are determined by errors in the quantities in (9). Estimated errors are f_i (15 % caused by the error in temperature at 25 K), ϕ_f(3 %), f_{gate} (3 %), S_i (5 %) and D (5 %, 1σ of values in Fig. 8), resulting in an absolute error for ϱ_{in} of $\sim$ 30 % (the relative error is smaller). Closer to the nozzle (at higher densities) the plot becomes non-linear, suggesting that the data analysis is underestimating the absolute density in this region. Indeed inspection of Fig. 13b indicates that the experimental density starts to fall below the value predicted by CFD as the nozzle is approached. Very close to the nozzle the radial width of the expansion, as predicted by CFD calculations, becomes small (see Fig. 12) and the barrel shock region may be probed by the laser, resulting in a larger error in the derived centreline density. Below densities of 9×10^{15} molecule cm^{-3}, the form of the Stern–Volmer plot (Fig. 14) was found to be independent of the gating parameters chosen, and indeed Fig. 14 is an average of data taken with long and short photon counter gates. Above this density the graph was nonlinear even for a short detection gate. The axial velocity of the beam, is predicted by CFD to have reached a fairly constant value of 700–750 m s^{-1} during this region, and hence any fly-out of excited OH from the volume imaged onto the PMT during the lifetime will be constant and cannot affect the slope of the graph. The value of k_{air}(26 K) is $\sim$ 4.3 times higher than the room temperature value of $\sim 6 \times 10^{-11}$ molecule^{-1} cm^3 s^{-1}, calculated from the known atmospheric composition (1 % water vapour) and quenching rate constants. At the low temperatures of the experiment, quenching is almost certainly from the lowest $N' = 0$, 1 levels following $Q_1(1)$ excitation, as the $N' = 1$ to $N' = 2$ separation within $A^2\Sigma^+ v' = 0$ is 34 cm^{-1} [46], larger than the likely collision energy. The quenching rate constant from $N' = 0$ or 1 will be slightly larger than the value from a thermally averaged distribution within $v' = 0$ at 300 K, but cannot explain the large increase in quenching observed between 300 and 26 K.

The rate of quenching is characterised by a phenomenological rate constant $k_{air}(T)$, which is a function of temperature only and is a measure of the rate of depletion of electronically excited OH:

$$\begin{aligned} -d[OH(A^2\Sigma^+)]/dt &= k_{air}(T)[OH(A^2\Sigma^+)][M{=}air] \\ &\quad + A_f[OH(A^2\Sigma^+)] \\ &= [Q_f(T) + A_f][OH(A^2\Sigma^+)]\,, \end{aligned} \tag{17}$$

where Q_f is the pseudo-first order quenching rate constant. At a molecular level the relative velocity of an OH-air (strictly the constituents of air) collision may take many values, and for each velocity a rate constant may be defined such that

$$k_q(v) = v\sigma_q(v)\,, \tag{18}$$

where $\sigma_q(v)$ is the velocity-dependent quenching cross-section. The thermal bulk rate constant is then given by

$$k_{air}(T) = \int v f(v) \sigma_q(v)\ dv \tag{19}$$

and for an isotropic sample at thermal equilibrium the form of $f(v)$ is given by the Maxwell-Boltzmann (MB) distribution. For free-jet expansions the distribution of relative velocities $f(v)$ is likely to be different in the axial and radial directions [50] (the bulk flow velocity in these directions is known

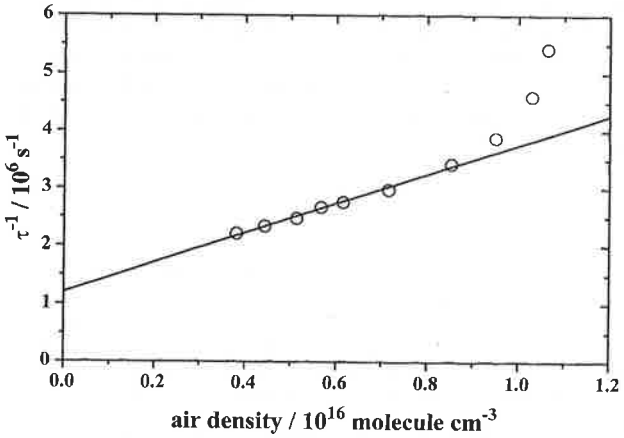

Fig. 14. A Stern–Volmer plot of the inverse fluorescence lifetime versus the jet density, for the region of the expansion inside the Mach disc where the temperature is approximately constant (average 26 K). The gradient yields a quenching rate constant of $(2.56 \pm 0.4) \times 10^{-10}$ molecule^{-1}cm^{3}s^{-1}, and an intercept (Einstein A coefficient) of $(1.2 \pm 0.3 \times 10^6$ s^{-1} (2σ error). The procedure for obtaining the absolute density is described in Sect. 2.2

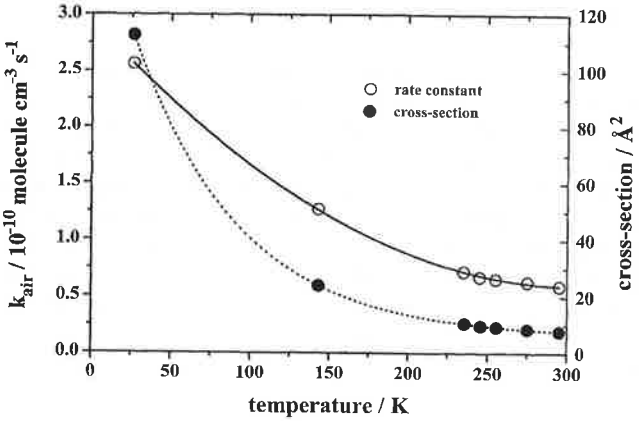

Fig. 15. Variation of quenching rate constant (open circles, left-hand axis) and cross-section (filled circles, right hand-axis) with temperature. The points at 26 and 143 K were obtained in this work from lifetime and density measurements within the supersonic expansion from a 1 mm nozzle, while the data between 230 and 300 K were obtained from lifetime measurements in a discharge-flow system [56]. The solid and dashed lines between data points are guides to the eye

to be different from the CFD calculations), with two temperatures describing the distributions. Furthermore, the radial distribution of velocities in some jet expansions has been calculated and shown not to be described by a MB distribution [9–11, 50], although the number densities are lower than used in this work. However, assuming an isotropic MB distribution (and the lifetime and rotational distributions support this), dividing the experimental value of $k_{air}(T)$ by the average velocity of an OH-air collision at the measured rotational temperature, yields an average cross-section $\sigma_R(T)$, which increases from 7.8 Å^2 at 300 K to 113 Å^2 at 26 K, an increase by a factor of 14.5. For the 1 mm nozzle expansion the rotational temperature was measured at one point in the Mach disc itself ($x = 24.5$ mm, $T = 143$ K), and from the density at this point (Fig. 9) a value of k_{air} was found to be 1.27×10^{-10} molecule^{-1} cm^3 s^{-1} or $\sigma_R = 23.9$ Å^2. Figure 15 shows the variation of the rate constant and cross-section for quenching of OH $A^2\Sigma^+$, v′= 0 by air between 26 and 300 K.

Rate constants for quenching of OH $A^2\Sigma^+$ by N_2, O_2, and H_2O at higher temperatures have been studied in laser-heated cells [28], flames [29], and shock tubes [30]. The values above room temperature change relatively little, and when combined with the low temperature data, the results overall are consistent with the dynamics of the quenching collisions being controlled by attractive features in potential energy surfaces between OH($A^2\Sigma^+$) and the major constituents of air. Such a finding is supported by the observation of relatively strongly bound OH($A^2\Sigma^+$) van der Waals molecules [57, 68–71] and *ab initio* calculations of the intermolecular potential energy surface for collisions of OH($A^2\Sigma^+$) [25, 26, 72]. Of all the atmospheric colliders, it is likely that the rate constant for quenching by water will increase most dramatically upon going to low temperatures. Further studies using expansions of pure gases containing known amounts of water vapour are underway in order to measure quenching rate constants for individual species over a wide range of temperatures. Smith and co-workers [9–11] have studied the velocity (and hence collision energy) dependence of ion–molecule charge-transfer reactions in jets. A difficult and detailed analysis was required to take of account of anisotropic velocity distributions [11] that were calculated for the experimental conditions. It is hoped that the mapping of the temperature and density profiles within the supersonic region of free-jets used in this work may allow the study of collisional processes of neutral species at ultralow temperatures without such an analysis, offering an alternative to the CRESU technique developed by Rowe and co-workers [22, 23]. The present technique should be widely applicable to the study of collisional processes of neutral excited states, but for ground state neutral species the limited observation time (determined by the transit time in the ultra-cold region of characterised temperature and density) will restrict study to very fast reactions or processes involving the main diluent gas.

5 Summary

A high-repetition rate laser system was utilised to probe the hydroxyl radical in supersonic expansions of irradiated air through a variety of pinhole and shaped nozzles. A detailed visualisation of both the OH rotational temperature and the air density within the expansion has aided greatly in the choice of design and operating conditions of an instrument to measure the concentrations of OH in the troposphere. The optimum signal for OH detection was obtained for a 1 mm nozzle, for which the background chamber pressure was 0.59 Torr, and when the laser beam was positioned to probe inside the supersonic part of the expansion. At this point cooling to a rotational temperature of 25 K was observed, and consequently the molecular partition function is minimised, with population maximised in the lowest rotational level that is probed by the laser. Over the region studied, the total OH density was highest downstream of the Mach disc in the sonic region of the expansion, demonstrating the importance of factors other than number density that determine the instrument sensitivity.

The absolute density of air in the beam was determined through calibration of the observed LIF signal by using OH fluorescence lifetimes at positions within the expansion where the quenching rate constant could be calculated. In this manner the air density profiles were mapped out for a variety of nozzles. Sharp gradients in temperature and density were found, with the position of the Mach disc shock being close to that predicted by simple theory. In addition a detailed CFD computation enabled a two-dimensional visualisation of the expansions to be obtained. Details of the expansion in the radial direction perpendicular to the gas flow were useful in confirming the absence of steep gradients in the volume that is probed by the laser, and which may lead to instabilities in OH measurements. Despite neglecting intermolecular forces and turbulent flow the CFD predictions along the centreline of the expansion were able to reproduce the salient features observed experimentally.

Knowledge of the absolute density of air across a region within the supersonic expansion where the rotational temperature was constant at ~ 25 K enabled kinetic studies to be performed. The environment was collisional, as confirmed by varying quantum yields for fluorescence between 0.2 and 0.6 in this region, and measurement of the lifetimes enabled the rate constant for quenching of the excited state of OH by air to be determined. Although some care must be exercised in the interpretation of a rate constant under conditions where the velocity distribution may be anisotropic, the value obtained is over 4 times higher than the value at 300 K, confirming the attractive nature of collisions of electronically excited OH. It is planned to study the collision dynamics of excited states with a variety of gases at ultra-low temperatures by this method, by using a variation of the expansion conditions to vary the temperature.

Acknowledgements. The authors wish to thank Dr. M.R. Heal (now at the University of Edinburgh) for assistance in the initial stages of this work, Mr. C. Reyner, Mr. P. Halford-Maw, and the School of Chemistry workshop staff for expert technical assistance, and Mr. M.T. Glossop for help in performing some of the experiments. The low temperature discharge-flow measurements of OH quenching were performed by Miss A.E. Bailey. Thanks are given to Dr. D.R. Crosley and Dr. J. Luque, of SRI International, for making available a copy of the LIFBASE spectral simulation package. The authors are also grateful to the NERC for support of the work (grant reference GST/02/10910), to the Royal Society for the award of a University Research Fellowship (DEH), to British Gas for a studentship (RF) during which the CFD code was written, and finally to The University of Leeds for the award of a University Scholarship (DJC) and funding for the CFD work through its Academic Development Fund.

References

1. J.B. Anderson: *In Molecular Beams and Low Density Gas Dynamics*, ed. by P.P. Wegener (Dekker, New York, 1974), p. 1; *Atomic and Molecular Beam Methods*, Volumes 1,2, ed. by G. Scoles (Oxford University Press, New York, 1988); J.C. Whitehead: Rep. Prog. Phys. **59**, 993 (1996); R.D. Levine, R.B. Bernstein: *Molecular Reaction Dynamics and Chemical Reactivity* (Oxford, New York, 1987)
2. K. Liu, R.G. Macdonald, A.F. Wagner: Int. Rev. Phys. Chem. **9**, 187 (1990); D. Bassi, A. Boschetti, S. Marchetti, G. Scoles, M. Zen: J. Chem. Phys. **74**, 2221 (1981); Y. Rudich, R.J. Gordon, E.E. Nikitin, R. Naaman: J. Chem. Phys. **96**, 4423 (1992); T.E. Gough, R.E. Miller: J. Chem. Phys. **78**, 4486 (1983)
3. M. Alagia, N. Balucani, P. Casavecchia, D. Stranges, G.G. Volpi: J. Chem. Soc. Far. Trans. **91**, 575 (1995)
4. D.H. Levy: Annu. Rev. Phys. Chem. **31**, 197 (1980); P.C. Engelking: Chem. Rev. **91**, 399 (1991); T.A. Miller: Science, **223**, 545 (1984)
5. M.P. Sinha, A. Schultz, R.N. Zare: J. Chem. Phys. **58**, 549 (1973); R.E. Smalley, L. Wharton, D.H. Levy: J. Chem. Phys. **63**, 4977 (1975); *ibid.* **64**, 3266 (1976)
6. Faraday Discussions of the Chemical Society, **97**, van der Waals molecules (1994)
7. M.C. Heaven: J. Phys. Chem. **97**, 8567 (1993); M.A. Suhm, D.J. Nesbitt: Chem. Soc. Rev. **24**, 45 (1995); R.C. Cohen, R.J. Saykally: J. Phys. Chem. **96**, 1024 (1992)
8. R.J. Bemish, M. Wu, R.E. Miller: Faraday Discussion **97**, 57 (1994)
9. M.A. Smith: *In Unimolecular and Bimolecular Reactions: Reaction Dynamics*, ed. by Baer and Powis (John Wiley, New York, 1984)
10. L.K. Randeniya, X.K. Zeng, M.A. Smith: Chem. Phys. Lett. **147**, 346 (1988); M. Hawley, T.L. Mazely, L.K. Randeniya, R.S. Smith, X.K. Zeng, M.A. Smith: Int. J. Mass. Spectrom. Ion Proc. **97**, 55 (1990); M. Hawley, M.A. Smith: J. Phys. Chem. **96**, 6693 (1992); M. Hawley, M.A. Smith: J. Chem. Phys. **95**, 8662 (1991)
11. T.L. Mazely, M.A. Smith: J. Chem. Phys. **89**, 2048 (1988); L.K. Randeniya, M.A. Smith: J. Chem. Phys. **93**, 661 (1990)
12. R. Cattolica, F. Robben, L. Talbot, D.R. Willis: Phys. Fluids, **17**, 1793 (1974)
13. M.R. Heal, D.E. Heard, M.J. Pilling, B.J. Whitaker: J. Atm. Sci. **52**, 3428 (1995)
14. A.D. Birch, D.R. Brown, M.G. Godson, F. Swaffield: Comb. Sci. Tech. **36**, 249 (1984)
15. G.W. Faris, R.L. Byer: Science, **238**, 1700 (1987)
16. S. Liu, Q. Zhang, C. Chen, Z. Zhang, J. Dai, X. Ma: J. Chem. Phys. **102**, 3617 (1995)
17. D.E. Heard, J.B. Jeffries, G.P. Smith, D.R. Crosley: Comb. and Flame, **88**, 137 (1992)
18. J.S. Bernstein, A. Fein, J.B. Choi, T.A. Cool, R.C. Sausa, S.L. Howard, R.L. Locke, A.W. Miziolek: Comb. Flame, **92**, 85 (1993)
19. A. Arnold, H. Becker, R. Hemberger, W. Hentschel, W. Ketterle, M. Kollner, W. Meienburg, P. Monkhouse, H. Neckel, M. Schafer, K.P. Schindler, V. Sick, R. Suntz, J. Wolfrum: Appl. Opt. **29**, 4860 (1990)
20. G.A. Raiche, J.B. Jeffries: Appl. Opt. **32**, 4629 (1993)
21. J.P. Booth, G. Hancock, N.D. Perry, M.J. Toogood: J. Appl. Phys. **66**, 5251 (1989)
22. B.R. Rowe, G. Dupeyrat, J.B. Marquette, P. Gaucherel: J. Chem. Phys. **80**, 4915 (1984); B.R. Rowe, J.B. Marquette, C. Rebrion: J. Chem. Soc. Faraday Trans. 2 **85**, 1631 (1989)
23. I.R. Sims, J.L. Queffelec, A. Defrance, C. Rebrion-Rowe, D. Travers, B.R. Rowe, I.W.M. Smith: J. Chem. Phys. **97**, 8798 (1992); I.R. Sims, J.-L. Queffelec, A. Defrance, C. Rebrion-Rowe, D. Travers, P. Bocherel, I.W.M. Smith: J. Chem. Phys. **100**, 4229 (1994)
24. D.C. Clary: Annu. Rev. Phys. Chem, **41**, 61 (1990); D.C. Clary, T.S. Stoecklin, A.G. Wickham: J. Chem. Soc. Far. Trans., **89**, 2185 (1993)
25. A. Degli Esposti, H.-J. Werner: J. Chem. Phys. **93**, 3351 (1990); A. Jörg, A. Degli Esposti, H.-J. Werner: J. Chem. Phys. **93**, 8757 (1990)
26. A Vegiri, S.C. Farantos: J. Phys. Chem. **92**, 2723 (1988)
27. R.A. Copeland, D.R. Crosley: J.Chem. Phys. **84**, 3099 (1986)
28. P.W. Fairchild, G.P. Smith, D.R. Crosley: J. Chem. Phys. **79**, 1795 (1983)
29. J.B. Jeffries, K. Koshe-Höinghaus, G.P. Smith, R.A. Copeland, D.R. Crosley: Chem. Phys. Lett. **152**, 160 (1988)
30. P.H. Paul, J.L. Durant Jr., J.A. Gray, M.R. Furlanetto: J. Chem. Phys. **102**, 8378 (1995)
31. T.M. Hard, R.J. O'Brien, C.Y. Chan, A.A. Mehrabzadeh: Environ. Sci. Technol. **18**, 768 (1984)
32. P.S. Stevens, J.H. Mather, W.H. Brune: J. Geophys. Res. **99, D2**, 3543 (1994)
33. F. Holland, M. Hessling, A. Hofzumahaus: J. Atm. Sci. **52**, 3393 (1995)
34. A. Hofzumahaus, U. Aschmutat, M. Hessling, F. Holland, D.H. Ehhalt: Geophys. Res. Lett. **23**, 2541 (1996)
35. D.J. Creasey, P. Halford-Maw, D.E. Heard, M.J. Pilling, J. Spence, B.J. Whitaker: manuscript in preparation, Meas. Sci. Technol.
36. K.R. German: J. Chem. Phys. **63**, 5252 (1975); *ibid.* **62**, 2584 (1975)
37. W.L. Dimpfl, J.L. Kinsey: J. Quant. Spectrosc. Radiat. **21**, 233 (1979)
38. P. Hogan, D.D. Davis: Chem. Phys. Lett, **29**, 255 (1974)
39. K.J. Rensberger, J.B. Jeffries, R.A. Copeland, K. Kohse-Höinghaus, M.L. Wise, D.R. Crosley: Appl. Opt. **28**, 3556 (1989)
40. I.L. Chidsey, D.R. Crosley: J. Quant. Spectrosc. Radiat. Transfer **23**, 187 (1980); D.R. Crosley, I.L. Chidsey: Ballistic Research Laboratory, Tables of Calculated Transition Probabilities for the A-X System of OH (1981)
41. J. Luque, D.R. Crosley: LIFBASE: Database and Spectral Simulation Program, SRI International, 1995
42. R.A. Copeland, M.J. Dyer, D.R. Crosley: J. Chem. Phys. **82**, 4022 (1985)
43. A. Jörg, U. Meier, R. Kienle, K. Kohse-Höinghaus: Appl. Phys. B, **55**, 305 (1992)
44. A. Jörg, U. Meier, K. Kohse-Höinghaus: J. Chem. Phys. **93**, 6453 (1990)
45. D.R. Crosley, R.K. Lengel: J. Quant. Spectrosc. Radiat. Transfer **15**, 579 (1975); J. Luque, D.R. Crosley, unpublished data
46. J.A. Coxon: Can. J. Phys. **58**, 933 (1980)
47. M.J. Weida, D.J. Nesbitt; J. Chem. Phys. **100**, 6372 (1994)
48. V. Aquilianti, D. Ascenzi, D. Cappelletti, F. Pirani: Nature, **371**, 399 (1994)
49. D.P. Pullman, D.R. Herschbach: J. Chem. Phys. **90**, 3881 (1989)
50. D.R. Miller: *In Atomic and Molecular Beam Methods*, ed. by G. Scoles (Oxford University Press, New York, 1988), p. 14
51. C.W. Bauschlicher Jr., S.R. Langhoff: J. Chem. Phys. **87**, 4665 (1987)
52. H.J. Werner, P. Rosmus: J. Chem. Phys. **80**, 831 (1984)
53. S.R. Langhoff, E.F. van Dishoeck, R. Wetmore, A. Dalgarno: J. Chem. Phys. **77**, 1379 (1982)
54. P. Andresen, N. Aristov, V. Beushausen, D. Häusler, H.W. Lülf: J. Chem. Phys. **95**, 5763 (1991)
55. I.J. Wysong, J.B. Jeffries, D.R. Crosley: J. Chem. Phys. **92**, 5218 (1990)
56. A.E. Bailey, D.E. Heard, P.H. Paul, M.J. Pilling: J. Chem. Soc. Faraday Trans., in press (1997)
57. L.C. Giancarlo, M.I. Lester: Chem. Phys. Lett. **240**, 1 (1995)
58. M.I. Lester: private communication (1995)
59. G.K. Batchelor: *Fluid Dynamics*, Cambridge University Press (1967)
60. C. Hirsch: *Numerical Computation of Internal and External Flows*, Vols. 1 and 2, (Wiley, Chichester, 1988, 1990)
61. R. Fairlie: *The effects on Structures due to Transient Compressible Flows*, Ph. D thesis, Department of Applied Mathematics, University of Leeds, UK (1995)
62. S.A.E.G. Falle: *Mon. Not. R. Astr. Soc.* **250**, 581 (1991)
63. S.K. Godunov: *Mat. Sb.* **47**, 271 (1959)
64. R.D. Richtmeyer, K.W. Morton: *Difference Methods for Initial-Value Problems* (Interscience, 2nd edition, 1967)
65. J.J. Gottlieb, C.P.T. Groth: *J. Comput. Phys.* **78**, 437 (1988)
66. E.F. Toro, C.C. Chou: *Int. J. Num. Meth. Fluids* **16**, 173 (1993)
67. P.W. Atkins: *Physical Chemistry*, 4th edition, (Oxford University Press, Oxford, 1990), Table 2.15
68. M.I. Lester, S.E. Choi, L.C. Giancarlo, R.W. Randall: Faraday Discuss. **97**, 365 (1994)
69. G.W. Lemire, R.C. Sausa: J. Phys. Chem. **96**, 4821 (1992)
70. M.C. Heaven: Annu. Rev. Phys. Chem. **43**, 283 (1992)
71. R.L. Schwartz, L.C. Giancarlo, R.A. Loomis, R.T. Boon, M.I. Lester: J. Chem. Phys. **105**, 10224 (1996)
72. M.I. Lester, R.A. Loomis, L.C. Giancarlo, M.T. Berry, C. Chakravarty, D.C. Clary: J. Chem. Phys. **98**, 9320 (1993)